

2005 ALCPG &amp; ILC Workshops - Snowmass, U.S.A.

## Report of the 2005 Snowmass Top/QCD Working Group

A. Juste<sup>a</sup>, Y. Kiyo<sup>b</sup>, F. Petriello<sup>c</sup>, T. Teubner<sup>d</sup>, K. Agashe<sup>e</sup>, P. Batra<sup>f</sup>, U. Baur<sup>g</sup>, C.F. Berger<sup>h</sup>, J.A.R. Cembranos<sup>i</sup>, A. Gehrmann-De Ridder<sup>j</sup>, T. Gehrmann<sup>k</sup>, E.W.N. Glover<sup>l</sup>, S. Godfrey<sup>m</sup>, A. Hoang<sup>n</sup>, M. Perelstein<sup>o</sup>, Z. Sullivan<sup>f</sup>, T. Tait<sup>f</sup>, S. Zhu<sup>p</sup>

This report discusses several topics in both top quark physics and QCD at an International Linear Collider (ILC). Issues such as measurements at the  $t\bar{t}$  threshold, including both theoretical and machine requirements, and the determination of electroweak top quark couplings are reviewed. New results concerning the potential of a 500 GeV  $e^+e^-$  collider for measuring  $Wtb$  couplings and the top quark Yukawa coupling are presented. The status of higher order QCD corrections to jet production cross sections, heavy quark form factors, and longitudinal gauge boson scattering, needed for percent-level studies at the ILC, are reviewed. A new study of the measurement of the hadronic structure of the photon at a  $\gamma\gamma$  collider is presented. The effects on top quark properties from several models of new physics, including composite models, Little Higgs theories, and CPT violation, are studied.

<sup>a</sup>Fermi National Accelerator Laboratory, P.O. Box 500, MS 357, Batavia, IL 60510, USA

<sup>b</sup>Institut für Theoretische Physik E, RWTH Aachen, D-52056 Aachen, Germany

<sup>c</sup>University of Wisconsin, Madison, WI 53706, USA *and* Fermi National Accelerator Laboratory, P.O. Box 500, MS 106, Batavia, IL 60510, USA

<sup>d</sup>Department of Mathematical Sciences, The University of Liverpool, Liverpool L69 3BX, England, U.K.

<sup>e</sup>Johns Hopkins University, Baltimore, MD 21218, USA *and* Institute for Advanced Studies, Princeton, NJ 08540, USA *and* Syracuse University, Syracuse, NY 13244, USA

<sup>f</sup>High Energy Physics Division, Argonne National Laboratory, Argonne, IL 60439, USA

<sup>g</sup>State University of New York at Buffalo, Buffalo, NY 14260, USA

<sup>h</sup>Stanford Linear Accelerator Center, Stanford University, Stanford, CA 94309, USA

<sup>i</sup>University of California, Irvine, CA 92697, USA

<sup>j</sup>Institut für Theoretische Physik, ETH, CH-8093 Zürich, Switzerland

<sup>k</sup>Institut für Theoretische Physik, Universität Zürich, CH-8057 Zürich, Switzerland

<sup>l</sup>Institute for Particle Physics Phenomenology, University Of Durham, Durham DH1 3LE, UK

<sup>m</sup>Ottawa Carleton Institute for Physics, Carleton University, Ottawa K1S 5B6, Canada

<sup>n</sup>Max-Planck-Institute for Physics, Munich, Germany

<sup>o</sup>CIHEP, Cornell University, Ithaca, NY 14853, USA

<sup>p</sup>Institute of Theoretical Physics, School of Physics, Peking University, Beijing 100871, China

## 1. INTRODUCTION

The precision study of both new and already discovered particles will be a major component of the experimental programs at both the Large Hadron Collider (LHC) and a future International Linear Collider (ILC). The past two decades in particle physics established the importance of this precision physics program. The outstanding success of the  $Z$ -pole program at LEP and SLC elevated the global fit to the precision electroweak data into the primary experimental constraint on extensions of the Standard Model (SM). When combined with input from the Tevatron, it probes energy scales far beyond the kinematic limits of current colliders.

The enormous production rates for top quarks at future colliders, reaching  $10^7$   $t\bar{t}$  pairs in a  $10\text{ fb}^{-1}$  year at the

LHC and  $10^5$  in a  $100 \text{ fb}^{-1}$  year at a 500 GeV  $e^+e^-$  collider, will allow a similar program studying the top quark to be pursued. Rare decays of the top quark, deviations from its chirality structure in the SM, and its electroweak couplings will be studied. A high precision measurement of the top quark mass will greatly reduce the uncertainties in important electroweak parameters. A variety of work is needed for this program to be successful, including the precision calculation of top quark properties in the SM, the determination of experimental capabilities for performing measurements, and finding the most likely deviations predicted by models of new physics. The calculation of higher-order QCD corrections to top quark cross sections can have an important effect on top quark physics; for example, the threshold corrections to the process  $e^+e^- \rightarrow t\bar{t}H$  increase its rate by a factor of two, drastically increasing the sensitivity of a 500 GeV ILC to the top quark Yukawa coupling (see Section 2.5 of this report). The precision needed for the  $t\bar{t}$  threshold scan imposes strong requirements on the monitoring of the luminosity spectrum, which are discussed in Section 2.7. Detailed analyses can reveal surprising experimental possibilities, such as the measurement of the  $Wtb$  coupling below the  $t\bar{t}$  threshold (see section 2.1 of this report). The study of the predictions coming from models of new physics show that the top quark can be a powerful discriminator between different theories; for example, composite theories such as the Randall-Sundrum model predict shifts in the coupling of right-handed top quarks to the  $Z$ , while Little Higgs models generically predict shifts in the left-handed top couplings (see Sections 4.1 and 4.2 of this report).

In addition to the study of the top quark, precision programs studying the Higgs boson or Higgs mechanism, the  $W$  and  $Z$  bosons, and other new particles discovered will be possible. To fully utilize the percent-level experimental precisions for each of these programs, higher order electroweak and QCD corrections in the SM must be included. For example, the two-loop QCD corrections to the  $g-2$  of the  $b$ -quark reach the 2–3% level, and must be included when studying  $b$  production during a Giga- $Z$  phase at the ILC (see Section 2.3 of this report). Benchmark processes for studying a strongly-interacting Higgs sector such as  $V_L V_L \rightarrow t\bar{t}$  receive QCD corrections reaching 10–20%, which can mask the effects of new physics if not taken into account (see Section 3.2 of this report). Finally, fundamental properties of QCD such as the running of the strong coupling constant and the hadronic structure of the photon can be studied with unprecedented precision (see Sections 3.1 and 3.3 of this report, respectively).

In this report we discuss several issues in top quark physics and precision QCD, with a focus on the physics program at the ILC. Section 2 discusses precision studies of the top quark at the ILC. Important issues such as the measurement of the  $t\bar{t}$  threshold cross section are reviewed, and new results such as the study of the  $Wtb$  coupling below the  $t\bar{t}$  threshold and the measurement of the top quark Yukawa at  $\sqrt{s} = 500$  GeV are presented. A preliminary study for the measurements of the average beam energy and luminosity spectrum at the ILC, needed for a precise  $t\bar{t}$  threshold scan, is presented in subsection 2.7. Section 3 discusses important QCD physics that can be performed at the ILC. Higher order QCD corrections needed for several important measurements are discussed, and new results for the determination of the hadronic structure of the photon are presented. Section 4 studies modifications of top quark properties in several models of new physics, and analyzes the potential of the ILC to measure these shifts and use them to discriminate between different extensions of the SM.

## 2. PRECISION STUDIES OF THE TOP QUARK AT THE ILC

### 2.1. Measuring the $Wtb$ Coupling Below the $t\bar{t}$ Threshold

*P. Batra, T. Tait*

A crucial test of the top quark's electroweak interactions is the strength of the charged current interaction  $W-t-b$ . In the Standard Model, unitarity of the CKM matrix implies that  $g_{Wtb} \sim gV_{tb} \sim g$ , but in extended models, including the simple extension by a fourth generation of fermions, this interaction can differ significantly from the SM expectation. Currently, it is known that the  $W-t-b$  vertex is sufficiently strong that the dominant top decay is  $t \rightarrow Wb$ , but even an imprecise measurement is lacking. Single top production at the Tevatron and LHC will help fill this gap in our knowledge, and is expected to lead to a measurement at the 10% level, dominated by systematics [1].

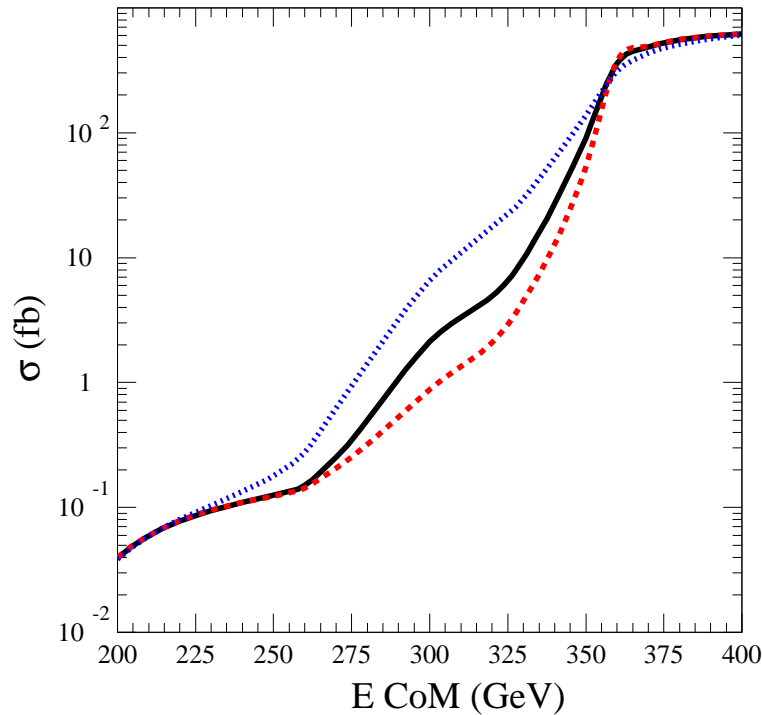


Figure 1: Inclusive rates for  $e^+e^- \rightarrow W^+bW^-\bar{b}$  as a function of the center-of-mass energy for  $g_{Wtb} = g_{SM}$  (black solid),  $g_{Wtb} = 2g_{SM}$  (blue dashed), and  $g_{Wtb} = g_{SM}/2$  (red dotted).

Unlike other top measurements, a direct test of  $W$ - $t$ - $b$  is challenging at the ILC. The current strategy is to perform a scan over the  $t\bar{t}$  threshold region, which is expected to yield precise measurements of many top parameters in the SM, including the top mass, width and Yukawa coupling (see [2] and this report for projections). Nevertheless, only an indirect measurement of the  $W$ - $t$ - $b$  coupling is offered above the  $t\bar{t}$  threshold, by inferring its value from the SM relation and a precise value of the top width. If, for example, there is a small non-standard decay mode of top, it will alter the width and distort the inferred coupling. It would be more desirable to have a direct measurement of  $W$ - $t$ - $b$ , by making use of a process which is directly proportional to it. Close to the  $t\bar{t}$  threshold, the sensitivity to the coupling is quite weak, because the rate is essentially the production cross section times the branching ratio for  $t \rightarrow Wb$ . Since we expect that the BR is very close to one, it does not in fact depend strongly on the magnitude of the  $W$ - $t$ - $b$  interaction.

Below the  $t\bar{t}$  threshold, the reaction  $e^+e^- \rightarrow W^+bW^-\bar{b}$  still occurs, through a mixture of non-resonant Feynman diagrams as well as through off-shell top quarks. At center-of-mass energies far enough below  $2m_t$  but still above  $m_t$ , the rate is dominated by contributions from the virtual  $t\bar{t}$  diagrams in a kinematic configuration where one top is on-shell and the other is off-shell. The rate becomes very sensitive to the  $W$ - $t$ - $b$  interaction, by virtue of the off-shell top [3]. This is illustrated in Figure 1, which plots the cross section as a function of energy for several values of  $g_{Wtb}$ , assuming a 175 GeV top mass and a 115 GeV Higgs mass. All analysis was performed using the MadEvent package [4] at tree level. The lines asymptote to the same value at both ends of the energy spectrum, as on-shell  $t\bar{t}$  production dominates close to threshold and graphs not involving top dominate far below threshold. Both of these extremes are independent of the  $W$ - $t$ - $b$  coupling. Thus, energies in between these two extremes are suitable to measure  $g_{Wtb}$ . We avoid the region very close to  $2m_t$  (despite its large rate), because the details of the transition from off-shell to

on-shell do depend sensitively on the top width, which could obscure  $g_{Wtb}$  if there are non-standard decay modes of the top. Instead, we focus on the energy  $\sqrt{s} = 340$  GeV, where good leverage on this coupling appears to be attained with small dependence on the width. We will explore the interplay between  $g_{Wtb}$  and  $\Gamma_t$  below.

Here we restrict ourselves to simple cuts to model the acceptance. To that end, we require the jets to have  $p_T > 10$  GeV and rapidities  $|y| < 2$ . We assume  $W$  bosons can be reconstructed with little background and for simplicity assume perfect  $b$ -tagging efficiency and no mis-tags. We improve the purity by requiring that one of the  $b$  quarks and one of the reconstructed  $W$ 's reconstruct an invariant mass within  $m_t \pm 10$  GeV, though we do not assume the charge of either the  $b$  or the  $W$  can be determined. The dominant background that is independent of the  $W$ - $t$ - $b$  coupling comes from diagrams with an intermediate Higgs, which can be eliminated by subtracting events with  $b\bar{b}$  that have an invariant mass close to the Higgs mass, once the mass is known. However, we do not impose such a cut in order to retain the most statistics possible.

The number of events will depend strongly on the top mass, the Higgs mass, the top width and  $g_{Wtb}$ . It is expected that the ILC will determine the top and Higgs masses to order 100 MeV or better, which is enough to render the uncertainty in the rates from these parameters much smaller than the expected statistical uncertainties. The remaining dependence on the width and  $g_{Wtb}$  allows us to determine a combination of both these quantities. To illustrate the results, we assume  $100 \text{ fb}^{-1}$  collected at  $\sqrt{s} = 340$  GeV. In Figure 2 we present the contours of constant event numbers in the plane of  $g_{Wtb}$  and  $\Gamma_t$  which reproduce the expected SM event rate of  $\sim 1500$  events. Also shown are the contours corresponding to  $1\sigma$  and  $2\sigma$  deviations from such a measurement (assuming that the SM rate is observed and considering purely statistical uncertainties). The result is the expected bound one would obtain on  $g_{Wtb}$  and  $\Gamma_t$ , which can be combined with the  $\Gamma_t$  from the above-threshold scan to extract  $g_{Wtb}$  itself (or alternately, one can go to lower energies where the sensitivity to  $\Gamma_t$  is less, though at the price of the loss of some statistics). From Figure 2, we see that assuming the width is measured with an uncertainty of 100 MeV,  $g_{Wtb}$  can be measured to the 2% level, which would represent better than a factor of 5 improvement compared to the LHC, and a major improvement in our understanding of the  $W$ - $t$ - $b$  interaction.

Many improvements on these rough estimates are possible. Certainly a more detailed and exhaustive study of the background would be interesting, as well as more sophisticated study of the signal, including higher order corrections and theory uncertainties, and detailed modelling of the  $W$  decays and the observability of the  $b$  quarks. In particular, higher order QCD and EW corrections to the signal will be essential to include in a realistic analysis in order to obtain the desired accuracy in  $g_{Wtb}$ , but are not likely to strongly change our conclusions as to how accurately one will be able to measure the coupling. Finally, since the cross section is strongly energy dependent, it could also be beneficial to consider the utility of a number of smaller data sets at several different energies below threshold. We leave such refinements for future work.

## 2.2. Probing Electroweak Top Quark Couplings at the ILC and the LHC

*U. Baur*

Although the top quark was discovered almost ten years ago [5, 6], many of its properties are still only poorly known [7]. In particular, the couplings of the top quark to the electroweak (EW) gauge bosons have not yet been directly measured. Current data provide only weak constraints on the couplings of the top quark with the EW gauge bosons, except for the  $ttZ$  vector and axial vector couplings which are rather tightly but indirectly constrained by LEP data; and the right-handed  $tbW$  coupling, which is severely bound by the observed  $b \rightarrow s\gamma$  rate [8].

At an  $e^+e^-$  linear collider with  $\sqrt{s} = 500$  GeV and an integrated luminosity of  $100 - 200 \text{ fb}^{-1}$  one can hope to measure the  $ttV$  ( $V = \gamma, Z$ ) couplings in top pair production with a few-percent precision [9]. However, the process  $e^+e^- \rightarrow \gamma^*/Z \rightarrow t\bar{t}$  is sensitive to both  $tt\gamma$  and  $ttZ$  couplings and significant cancellations between the various couplings can occur. At hadron colliders,  $t\bar{t}$  production is so dominated by the QCD processes  $q\bar{q} \rightarrow g^* \rightarrow t\bar{t}$  and  $gg \rightarrow t\bar{t}$  that a measurement of the  $tt\gamma$  and  $ttZ$  couplings via  $q\bar{q} \rightarrow \gamma^*/Z^* \rightarrow t\bar{t}$  is hopeless. Instead, the  $ttV$  couplings can be measured in QCD  $t\bar{t}\gamma$  production, radiative top quark decays in  $t\bar{t}$  events ( $t\bar{t} \rightarrow \gamma W^+ W^- b\bar{b}$ ), and QCD  $t\bar{t}Z$  production [10].  $t\bar{t}\gamma$  production and radiative top quark decays are sensitive only to the  $tt\gamma$  couplings, whereas  $t\bar{t}Z$

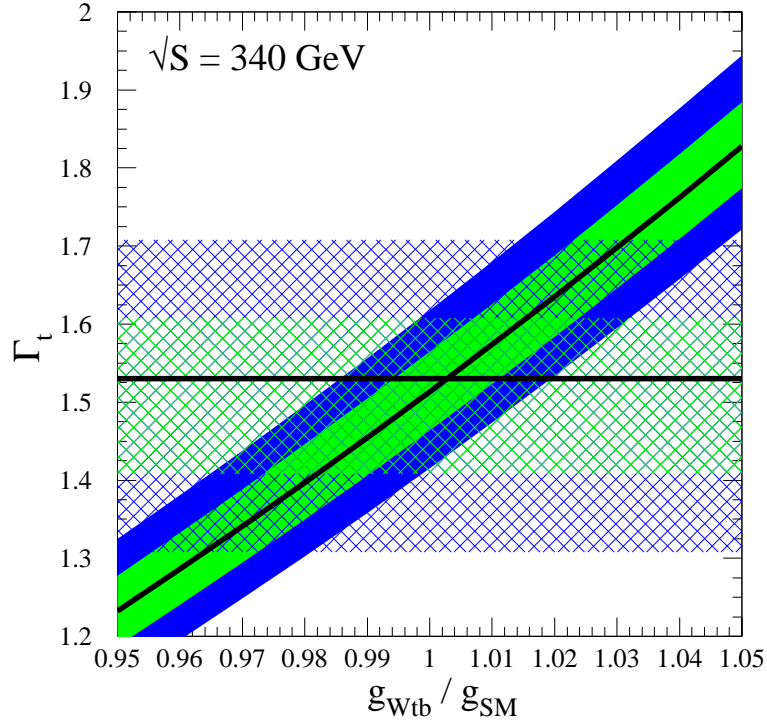


Figure 2: Curve corresponding to the SM rate and its  $1\sigma$  and  $2\sigma$  deviations in the plane of  $g_{Wtb}$  and  $\Gamma_t$ . Also overlaid is an expected measurement of  $\Gamma_t$  from the on-shell threshold scan with an uncertainty of 100 MeV.

production gives information only on the structure of the  $ttZ$  vertex. This obviates having to disentangle potential cancellations between the different couplings. In this section we briefly review the measurement of the  $ttV$  couplings at the LHC and compare the expected sensitivities with the bounds which one hopes to achieve at an  $e^+e^-$  linear collider.

The most general Lorentz-invariant vertex function describing the interaction of a neutral vector boson  $V$  with two top quarks can be written in terms of ten form factors [11], which are functions of the kinematic invariants. In the low energy limit, these correspond to couplings which multiply dimension-four or -five operators in an effective Lagrangian, and may be complex. If  $V$  is on-shell, or if  $V$  couples to effectively massless fermions, the number of independent form factors is reduced to eight. If, in addition, both top quarks are on-shell, the number is further reduced to four. In this case, the  $ttV$  vertex can be written in the form

$$\Gamma_\mu^{ttV}(k^2, q, \bar{q}) = -ie \left\{ \gamma_\mu (F_{1V}^V(k^2) + \gamma_5 F_{1A}^V(k^2)) + \frac{\sigma_{\mu\nu}}{2m_t} (q + \bar{q})^\nu (iF_{2V}^V(k^2) + \gamma_5 F_{2A}^V(k^2)) \right\}, \quad (1)$$

where  $e$  is the proton charge,  $m_t$  is the top quark mass,  $q$  ( $\bar{q}$ ) is the outgoing top (anti-top) quark four-momentum, and  $k^2 = (q + \bar{q})^2$ . The terms  $F_{1V}^V(0)$  and  $F_{1A}^V(0)$  in the low energy limit are the  $ttV$  vector and axial vector form factors. The coefficients  $F_{2V}^{\gamma}(0)$  and  $F_{2A}^{\gamma}(0)$  are related to the magnetic and ( $CP$ -violating) electric dipole form factors.

In  $t\bar{t}V$  production, one of the top quarks coupling to  $V$  is off-shell. The most general vertex function relevant for  $t\bar{t}V$  production thus contains additional couplings, not included in Eq. (1). These additional couplings are irrelevant in  $e^+e^- \rightarrow t\bar{t}$ , where both top quarks are on-shell.

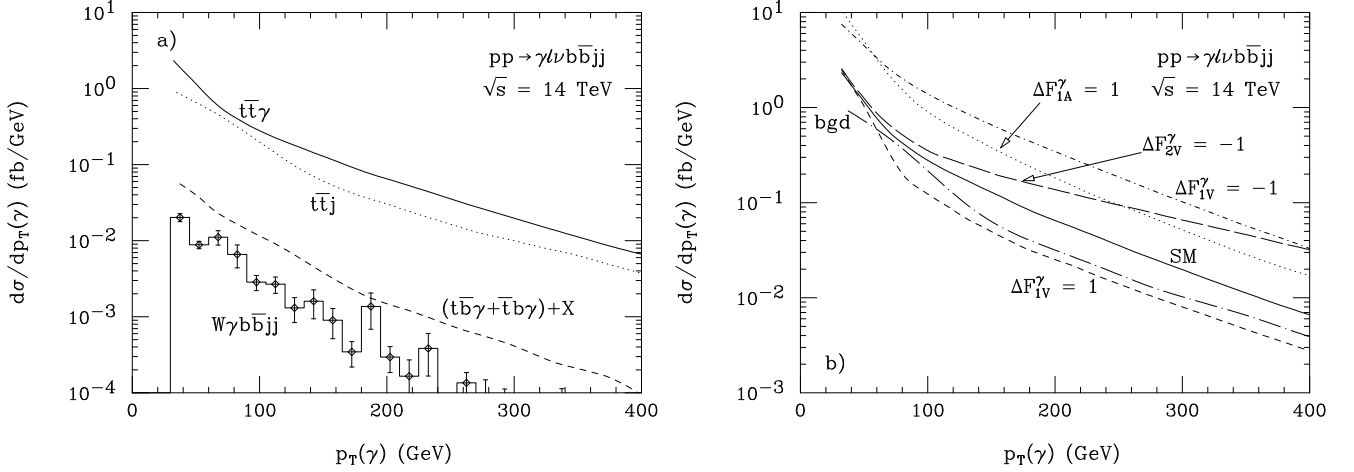


Figure 3: The differential cross sections as a function of the photon transverse momentum for  $\gamma\ell\nu_i b\bar{b}jj$  production at the LHC. Part a) shows the SM signal and the various contributions to the background. Part b) shows the SM signal and background, and the signal for various anomalous  $tt\gamma$  couplings.

In  $e^+e^- \rightarrow t\bar{t}$  one often uses the following parameterization for the  $ttV$  vertex:

$$\Gamma_{\mu}^{ttV}(k^2, q, \bar{q}) = ie \left\{ \gamma_{\mu} \left( \tilde{F}_{1V}^V(k^2) + \gamma_5 \tilde{F}_{1A}^V(k^2) \right) + \frac{(q - \bar{q})_{\mu}}{2m_t} \left( \tilde{F}_{2V}^V(k^2) + \gamma_5 \tilde{F}_{2A}^V(k^2) \right) \right\}. \quad (2)$$

Using the Gordon decomposition, it is easy to show that Eqs. (1) and (2) are equivalent for on-shell top quarks and that the form factors  $\tilde{F}_{iV,A}^V$  and  $F_{iV,A}^V$  ( $i = 1, 2$ ) are related by

$$\tilde{F}_{1V}^V = - (F_{1V}^V + F_{2V}^V), \quad \tilde{F}_{2V}^V = F_{2V}^V, \quad \tilde{F}_{1A}^V = -F_{1A}^V, \quad \tilde{F}_{2A}^V = -iF_{2A}^V. \quad (3)$$

The most promising channel for measuring the  $tt\gamma$  couplings at the LHC is  $pp \rightarrow \gamma\ell\nu_i b\bar{b}jj$  which receives contributions from  $t\bar{t}\gamma$  production and ordinary  $t\bar{t}$  production where one of the top quarks decays radiatively,  $t \rightarrow Wb\gamma$ . In order to reduce the background, it is advantageous to require that both  $b$ -quarks are tagged. We assume a combined efficiency of  $\epsilon_b^2 = 40\%$  for tagging both  $b$ -quarks.

The non-resonant  $pp \rightarrow W(\rightarrow \ell\nu)\gamma b\bar{b}jj$  background and the single-top backgrounds,  $(t\bar{b}\gamma + \bar{t}b\gamma) + X$ , can be suppressed by imposing invariant and transverse mass cuts which require that the event is consistent either with  $t\bar{t}\gamma$  production, or with  $t\bar{t}$  production with radiative top decay [10]. Imposing a large separation cut of  $\Delta R(\gamma, b) > 1$  reduces photon radiation from the  $b$  quarks. Photon emission from  $W$  decay products can essentially be eliminated by requiring that  $m(jj\gamma) > 90$  GeV and  $m_T(\ell\gamma; \not{p}_T) > 90$  GeV, where  $m(jj\gamma)$  is the invariant mass of the  $jj\gamma$  system, and  $m_T(\ell\gamma; \not{p}_T)$  is the  $\ell\gamma\not{p}_T$  cluster transverse mass, which peaks sharply at  $m_W$ . After imposing the cuts described above, the irreducible backgrounds are one to two orders of magnitude smaller than the signal.

The potentially most dangerous reducible background is  $t\bar{t}j$  production where one of the jets in the final state fakes a photon. In Fig. 3a we show the photon transverse momentum distributions of the  $t\bar{t}\gamma$  signal and the backgrounds discussed above. The  $t\bar{t}j$  background is seen to be a factor 2 to 3 smaller than the  $t\bar{t}\gamma$  signal for the jet - photon misidentification probability ( $P_{j \rightarrow \gamma} = 1/1600$  [12]) used.

The photon transverse momentum distributions in the SM and for various anomalous  $tt\gamma$  couplings, together with the  $p_T(\gamma)$  distribution of the background, are shown in Fig. 3b. Only one coupling at a time is allowed to deviate from its SM prediction.

The process  $pp \rightarrow t\bar{t}Z$  leads to either  $\ell'^+ \ell'^- \ell\nu b\bar{b}jj$  or  $\ell'^+ \ell'^- b\bar{b} + 4j$  final states if the  $Z$ -boson decays leptonically and one or both of the  $W$  bosons decay hadronically. If the  $Z$  boson decays into neutrinos and both  $W$  bosons decay hadronically, the final state consists of  $\not{p}_T b\bar{b} + 4j$ . Since there is essentially no phase space for  $t \rightarrow WZb$  decays ( $BR(t \rightarrow WZb) \approx 3 \cdot 10^{-6}$  [13]), these final states arise only from  $t\bar{t}Z$  production.

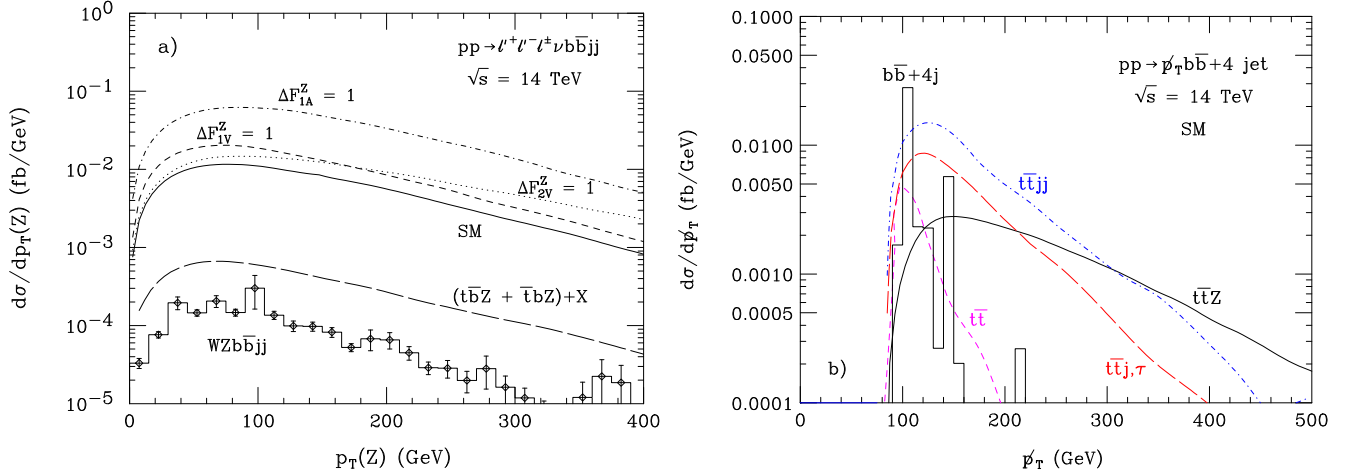


Figure 4: a) The differential cross sections at the LHC as a function of  $p_T(Z)$  for  $\ell'^+\ell'^-\ell\nu b\bar{b}jj$  final states. Shown are the SM predictions for  $t\bar{t}Z$  production, for several non-standard  $ttZ$  couplings, and for various backgrounds. Only one coupling at a time is allowed to deviate from its SM value. b) The differential cross sections as a function of the missing transverse momentum for  $p_T b\bar{b} + 4j$  production at the LHC. Shown are the SM predictions for  $t\bar{t}Z$  production and for various backgrounds.

In order to identify leptons,  $b$  quarks, light jets and the missing transverse momentum in dilepton and trilepton events, the same cuts as for  $t\bar{t}\gamma$  production are imposed. One also requires that there is a same-flavor, opposite-sign lepton pair with invariant mass near the  $Z$  resonance,  $m_Z - 10 \text{ GeV} < m(\ell\ell) < m_Z + 10 \text{ GeV}$ .

The main backgrounds contributing to the trilepton final state are singly-resonant  $(t\bar{b}Z + \bar{t}bZ) + X$  ( $t\bar{b}Zjj$ ,  $\bar{t}bZjj$ ,  $t\bar{b}Z\ell\nu$  and  $\bar{t}bZ\ell\nu$ ) and non-resonant  $WZb\bar{b}jj$  production. In the dilepton case, the main background arises from  $Zb\bar{b} + 4j$  production. To adequately suppress it, one additionally requires that events have at least one combination of jets and  $b$  quarks which is consistent with the  $b\bar{b} + 4j$  system originating from a  $t\bar{t}$  system. Once these cuts have been imposed, the  $Zb\bar{b} + 4j$  background is important only for  $p_T(Z) < 100 \text{ GeV}$ .

The  $Z$  boson transverse momentum distribution for the trilepton final state is shown in Fig. 4a for the SM signal and backgrounds, as well as for the signal with several non-standard  $ttZ$  couplings. Only one coupling at a time is allowed to deviate from its SM prediction. The backgrounds are each more than one order of magnitude smaller than the SM signal. Note that varying  $F_{IV,A}^Z$  leads mostly to a cross section normalization change, hardly affecting the shape of the  $p_T(Z)$  distribution.

For the  $p_T b\bar{b} + 4j$  [14] final state at least 3 jets with  $p_T > 50 \text{ GeV}$  and  $p_T > 5 \text{ GeV}^{1/2} \sqrt{\sum p_T}$  are required. The largest backgrounds for this final state come from  $t\bar{t}$  and  $b\bar{b} + 4j$  production where one or several jets are badly mismeasured, from  $pp \rightarrow t\bar{t}jj$  with  $t\bar{t} \rightarrow \ell^\pm \nu_\ell b\bar{b}jj$  and the charged lepton being missed, and from  $t\bar{t}j$  production, where one top decays hadronically,  $t \rightarrow Wb \rightarrow bjj$ , and the other via  $t \rightarrow Wb \rightarrow \tau\nu_\tau b$  with the  $\tau$ -lepton decaying hadronically,  $\tau \rightarrow h\nu_\tau$ .

In Fig. 4b we show the missing transverse momentum distributions of the SM  $t\bar{t}Z \rightarrow p_T b\bar{b} + 4j$  signal (solid curve) and various backgrounds. The most important backgrounds are  $t\bar{t}jj$  and  $t\bar{t}j$  production. However, the missing transverse momentum distribution from these processes falls considerably faster than that of the signal, and for  $p_T > 300 \text{ GeV}$ , the SM signal dominates.

The shape and normalization changes of the photon or  $Z$ -boson transverse momentum distribution can be used to derive quantitative sensitivity bounds on the anomalous  $tt\gamma$  and  $ttZ$  couplings. For  $t\bar{t}Z$  production with  $Z \rightarrow \ell'^+\ell'^-$ , the  $\Delta\Phi(\ell'\ell')$  distribution provides additional information [10]. In the following we assume a normalization uncertainty of the SM cross section of  $\Delta\mathcal{N} = 30\%$ .

Even for a modest integrated luminosity of  $30 \text{ fb}^{-1}$ , it will be possible to measure the  $tt\gamma$  vector and axial vector couplings, and the dipole form factors, with a precision of typically 20% and 35%, respectively. For  $300 \text{ fb}^{-1}$ , the

Table I: Sensitivities achievable at 68.3% CL for the anomalous  $ttV$  ( $V = \gamma, Z$ ) couplings  $\tilde{F}_{1V,A}^V$  and  $\tilde{F}_{2V,A}^V$  of Eq. (2) at the LHC for integrated luminosities of  $300 \text{ fb}^{-1}$ , and the ILC with  $\sqrt{s} = 500 \text{ GeV}$  (taken from Ref. [9]). Only one coupling at a time is allowed to deviate from its SM value.

coupling	LHC, $300 \text{ fb}^{-1}$	$e^+e^-$ [9]	coupling	LHC, $300 \text{ fb}^{-1}$	$e^+e^-$ [9]
$\Delta\tilde{F}_{1V}^\gamma$	+0.043 -0.041	+0.047, 200 $\text{fb}^{-1}$ -0.047, 200 $\text{fb}^{-1}$	$\Delta\tilde{F}_{1V}^Z$	+0.24 -0.62	+0.012, 200 $\text{fb}^{-1}$ -0.012, 200 $\text{fb}^{-1}$
$\Delta\tilde{F}_{1A}^\gamma$	+0.051 -0.048	+0.011, 100 $\text{fb}^{-1}$ -0.011, 100 $\text{fb}^{-1}$	$\Delta\tilde{F}_{1A}^Z$	+0.052 -0.060	+0.013, 100 $\text{fb}^{-1}$ -0.013, 100 $\text{fb}^{-1}$
$\Delta\tilde{F}_{2V}^\gamma$	+0.038 -0.035	+0.038, 200 $\text{fb}^{-1}$ -0.038, 200 $\text{fb}^{-1}$	$\Delta\tilde{F}_{2V}^Z$	+0.27 -0.19	+0.009, 200 $\text{fb}^{-1}$ -0.009, 200 $\text{fb}^{-1}$
$\Delta\tilde{F}_{2A}^\gamma$	+0.16 -0.17	+0.014, 100 $\text{fb}^{-1}$ -0.014, 100 $\text{fb}^{-1}$	$\Delta\tilde{F}_{2A}^Z$	+0.28 -0.27	+0.052, 100 $\text{fb}^{-1}$ -0.052, 100 $\text{fb}^{-1}$

limits improve to 4 – 7% for  $F_{1V,A}^\gamma$  and to about 20% for  $F_{2V,A}^\gamma$ . At the SLHC, assuming an integrated luminosity of  $3000 \text{ fb}^{-1}$ , one can hope to achieve a 2 – 3% measurement of the vector and axial vector couplings, and a 10% measurement of  $F_{2V,A}^\gamma$ , provided that particle identification efficiencies are not substantially smaller, and the reducible backgrounds not much larger, than what we have assumed.

To extract bounds on the  $ttZ$  couplings, we perform a simultaneous fit to the  $p_T(Z)$  and the  $\Delta\Phi(\ell'\ell')$  distributions for the trilepton and dilepton final states, and to the  $\not{p}_T$  distribution for the  $\not{p}_T b\bar{b} + 4j$  final state. We calculate sensitivity bounds for  $300 \text{ fb}^{-1}$  and  $3000 \text{ fb}^{-1}$  at the LHC; for  $30 \text{ fb}^{-1}$  the number of events expected is too small to yield meaningful results. For an integrated luminosity of  $300 \text{ fb}^{-1}$ , it will be possible to measure the  $ttZ$  axial vector coupling with a precision of 10 – 12%, and  $F_{2V,A}^Z$  with a precision of 40%. At the SLHC, these bounds can be improved by factors of about 1.6 ( $F_{2V,A}^Z$ ) and 3 ( $F_{1A}^Z$ ). The bounds which can be achieved for  $F_{1V}^Z$  are much weaker than those projected for  $F_{1A}^Z$ . As mentioned in Sec. 4, the  $p_T(Z)$  distributions for the SM and for  $F_{1V,A}^Z = -F_{1V,A}^{Z,SM}$  are almost degenerate. This is also the case for the  $\Delta\Phi(\ell'\ell')$  distribution. In a fit to these two distributions, therefore, an area centered at  $\Delta F_{1V,A}^Z = -2F_{1V,A}^{Z,SM}$  remains which cannot be excluded, even at the SLHC. For  $F_{1V}^Z$ , the two regions merge, resulting in rather poor limits.

It is instructive to compare the bounds for anomalous  $ttV$  couplings achievable at the LHC with those projected for the ILC. The most complete study of  $t\bar{t}$  production at the ILC for general  $ttV$  ( $V = \gamma, Z$ ) couplings so far is that of Ref. [9]. It uses the parameterization of Eq. (2) for the  $ttV$  vertex function. In order to compare the bounds of Ref. [9] with those anticipated at the LHC, the limits on  $F_{1V,A}^V$  and  $F_{2V,A}^V$  have to be converted into bounds on  $\tilde{F}_{1V,A}^V$  and  $\tilde{F}_{2V,A}^V$ . Table I compares the bounds we obtain for  $\tilde{F}_{1V,A}^V$  and  $\tilde{F}_{2V,A}^V$  with those reported for the ILC in Ref. [9]. Note that only one coupling at a time is allowed to deviate from its SM value [9]. We show LHC limits only for an integrated luminosity of  $300 \text{ fb}^{-1}$ . For the SLHC, with  $3000 \text{ fb}^{-1}$ , we obtain bounds which are a factor 1.3 – 3 more stringent than those shown in Table I. Thus, even if the SLHC operates first, and the  $\not{p}_T b\bar{b} + 4j$  final state is taken into account, a linear collider will still be able to significantly improve the  $ttZ$  anomalous coupling limits, with the possible exception of  $\tilde{F}_{1A}^Z$ . The ILC will also be able to considerably strengthen the bounds on  $\tilde{F}_{1A}^\gamma$  and  $\tilde{F}_{2A}^\gamma$ . It should be noted, however, that this picture could change once correlations between different non-standard  $ttZ$  couplings, and between  $tt\gamma$  and  $ttZ$  couplings, are taken into account. Unfortunately, so far no realistic studies for  $e^+e^- \rightarrow t\bar{t}$  which include these correlations have been performed.

The LHC will be able to perform first tests of the  $ttV$  couplings. Already with an integrated luminosity of  $30 \text{ fb}^{-1}$ , one can probe the  $tt\gamma$  couplings with a precision of about 10 – 35% per experiment. With higher integrated luminosities one will be able to reach the few percent region. With the exception of  $F_{1A}^Z$ , the  $ttZ$  couplings can only be measured with a precision of 15 – 50%, even at the SLHC. The ILC will be able to further improve our knowledge of the  $ttV$  couplings, in particular in the  $ttZ$  case.

### 2.3. Two-loop Corrections to Heavy Quark Form Factors

*T. Gehrmann*

The international linear collider will produce large numbers of top-antitop quark pairs, thus allowing for precision studies of the properties of the top quark. These experimental precision studies require equally precise theoretical predictions, i.e. higher order corrections in perturbation theory. Up to now, the theoretical effort was focused on a precise description of top quark production at threshold (see [15] for a review), where QCD corrections to next-to-next-to-leading order (NNLO) in perturbation theory are known, while observables other than the total production cross section in the continuum are known only to next-to-leading order (NLO) accuracy. In this section, we present results on the virtual two-loop corrections to vertex functions involving heavy quarks, which are an important ingredient to the NNLO corrections to top quark observables in the continuum.

The vertex function coupling an on-shell heavy quark antiquark pair to an external current can be decomposed into so-called form factors, whose coefficients follow from Lorentz invariance and symmetry properties of the current. For the vector and axial vector current (electroweak gauge boson), the vertex function contains, within QCD, four form factors ( $F_{1,2}$ ,  $G_{1,2}$ ):

$$\begin{aligned}
 \begin{array}{c} p_1 \\ \swarrow \\ \gamma, Z^0 \\ \searrow \\ p_2 \end{array} &= (-i) \left( v_Q F_1(s, m^2) \gamma^\mu + v_Q \frac{1}{2m} F_2(s, m^2) i \sigma^{\mu\nu} (p_1 + p_2)_\nu \right. \\
 &\quad \left. + a_Q G_1(s, m^2) \gamma^\mu \gamma_5 + a_Q \frac{1}{2m} G_2(s, m^2) \gamma_5 (p_1 + p_2)^\mu \right).
 \end{aligned}$$

The coupling of heavy quarks to Higgs bosons of positive and negative parity contains the scalar and pseudoscalar form factors:

$$\begin{array}{c} p_1 \\ \swarrow \\ H, A \\ \searrow \\ p_2 \end{array} = -i \frac{m}{v} [S_Q F_S(s, m^2) + i P_Q F_P(s, m^2) \gamma_5]$$

Here  $s$  is the invariant momentum squared of the external current and  $m$  the heavy quark mass.

The two-loop corrections to the form factors are obtained by applying appropriate projections to the Feynman diagrams displayed in Figure 5. As a result, the form factors are expressed in terms of hundreds of different scalar integrals. These integrals are reduced to a small set of master integrals by means of the so-called Laporta algorithm [16] with the help of integration-by-parts identities [17] and Lorentz-invariance identities [18]. The master integrals themselves were evaluated with the method of differential equations [18, 19, 20, 21] in [22, 23]. The master integrals, and thus the form factors are represented as series in the regularization parameter  $\epsilon$  and expressed in terms of 1-dimensional harmonic polylogarithms up to weight 4 [24, 25].

We obtained the complete two-loop corrections for the renormalized vector [26], axial-vector [27, 28], scalar and pseudoscalar [29] form factors. Agreement was found with earlier partial results and with expansions around special kinematical points.

An immediate physical application of the QCD corrections to the heavy quark form factors for arbitrary momentum transfer are predictions for form factors at zero recoil, the so-called static form factors.

Measurements of these static form factors for heavy quarks could allow indirect constraints on new physics scenarios. Recently, there has been considerable effort to determine the feasibility of such experimental measurements. Specifically, the couplings to photons and  $Z$  bosons have been studied in detail – both for heavy quark production at hadron colliders [10, 30] and at a future high-luminosity high-energetic linear electron-positron collider [9, 31, 32]. At this workshop, this issue was revisited in great depth especially in view of discriminating new physics scenarios [33].

The most prominent static form factor is the electromagnetic spin-flipping form factor: the anomalous magnetic moment, which is finite in the zero-recoil limit, and can be obtained from the results of the previous section [34]. It reads

$$F_{2,Q}(s=0) = \frac{\alpha_s}{2\pi} C_F + \left( \frac{\alpha_s}{2\pi} \right)^2 F_{2,Q}^{(2l)},$$

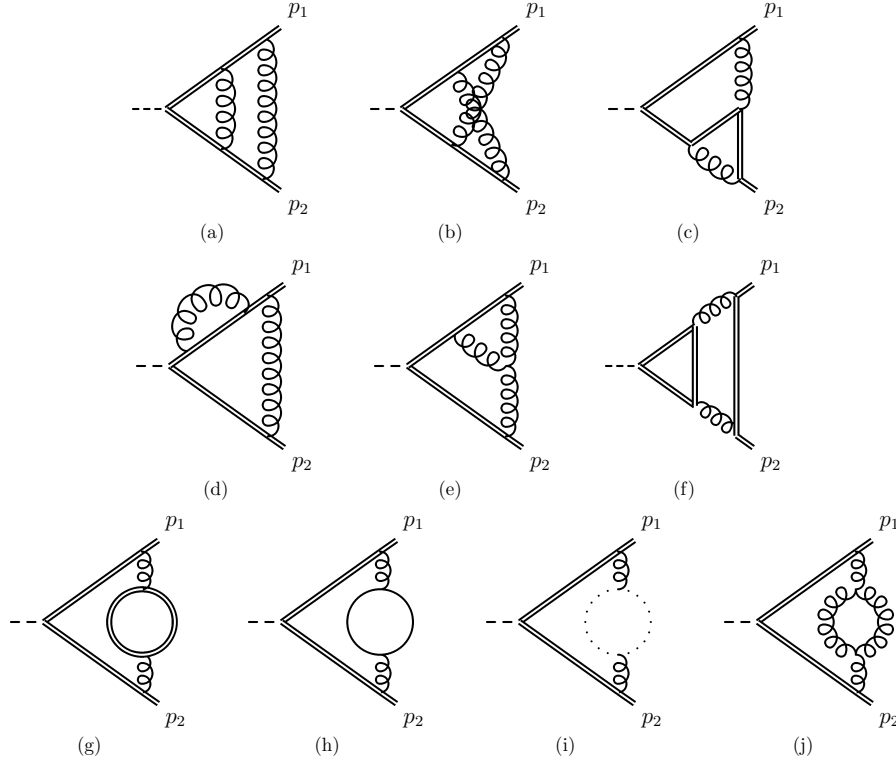


Figure 5: Feynman diagrams contributing to the two-loop QCD corrections to heavy quark form factors

	$t (\mu = m_t)$	$b (\mu = m_b)$	$b (\mu = m_Z)$
$(g-2)_Q^{\gamma,(1l)}/2$	$1.53 \cdot 10^{-2}$	$-1.52 \cdot 10^{-2}$	$-8.4 \cdot 10^{-3}$
$(g-2)_Q^{\gamma,(2l)}/2$	$4.7 \cdot 10^{-3}$	$-1.00 \cdot 10^{-2}$	$-6.6 \cdot 10^{-3}$
$(g-2)_Q^{\gamma}/2$	$2.00 \cdot 10^{-2}$	$-2.52 \cdot 10^{-2}$	$-1.50 \cdot 10^{-2}$
$(g-2)_Q^{Z,(1l)}/2$	$5.2 \cdot 10^{-3}$	$-1.87 \cdot 10^{-2}$	$-1.03 \cdot 10^{-2}$
$(g-2)_Q^{Z,(2l)}/2$	$1.6 \cdot 10^{-3}$	$-1.24 \cdot 10^{-2}$	$-8.1 \cdot 10^{-3}$
$(g-2)_Q^Z/2$	$6.8 \cdot 10^{-3}$	$-3.11 \cdot 10^{-2}$	$-1.85 \cdot 10^{-2}$

 Table II: One- and two-loop QCD contributions, and their sums, to the anomalous magnetic and weak magnetic moments of the top and bottom quark, for different values of the renormalization scale  $\mu$ .

with

$$\begin{aligned}
 F_{2,Q}^{(2l)} = & C_F^2 \left( -\frac{31}{4} + 2\zeta_2(5 - 6 \ln(2)) + 3\zeta_3 \right) + C_F C_A \left( \frac{317}{36} + 3\zeta_2(-1 + 2 \ln(2)) - \frac{3}{2}\zeta_3 \right) \\
 & + C_F T_F \left( \frac{119}{9} - 8\zeta_2 \right) - \frac{25}{9} C_F T_F N_l + C_F \beta_0 \ln(\mu^2/m_Q^2),
 \end{aligned}$$

from which we can derive the static magnetic and weak magnetic form factor of a quark  $Q$ . We consider

$$\left( \frac{g-2}{2} \right)_Q^{\gamma,Z} \equiv F_{2,Q}^{\gamma,Z}(0) = v_Q^{\gamma,Z} F_{2,Q}(0),$$

which correspond to the anomalous magnetic (MDM) and weak magnetic (WMDM) moments of  $Q$ . (Notice that in the literature the WMDM is often associated with  $F_{2,Q}^Z(s=m_Z^2)$ .) Numerical values for  $t$  and  $b$  quarks are given in Table II.

For the  $b$  quark an upper bound on its magnetic moment was derived in [35] from an analysis of LEP1 data, which, in our convention, reads  $\delta(g-2)_b^\gamma/2 < 1.5 \times 10^{-2}$  (68 % C.L.). Comparing it with Table II we see that

the QCD-induced contributions to the  $b$  quark magnetic moment saturate this bound, which implies that there is limited room for new physics contributions to this quantity. At a future linear collider [9, 32], when operated at the  $Z$  resonance, the sensitivity to this variable could be improved substantially, either by global fits or by analyzing appropriate angular distributions in  $b\bar{b}$  and  $b\bar{b}\gamma$  events.

As to the static form factors of the top quark, no such tight constraints exist so far on possible contributions from new interactions (see [10] for a review). These quantities are particularly sensitive to the dynamics of electroweak symmetry breaking. For instance, in various models with a strongly coupled symmetry breaking sector one may expect contributions from this sector to the static  $t$  quark form factors at the 5 - 10 % level [33]. The QCD-induced anomalous magnetic moment and the QCD corrections to the axial charge of the top quark are of the same order of magnitude. Future colliders have the potential to reach this level of sensitivity.

The form factors presented here have a number of applications, which will be addressed in future work. The vector and axial vector form factors contribute to the NNLO corrections to the forward-backward asymmetry for heavy quarks; they can also be used to compute the differential top quark pair production cross section at the ILC in the continuum, where top quark mass effects are still non-negligible. The scalar and pseudoscalar form factors enter the NNLO corrections to the decay of a Higgs boson into heavy quarks. These would become especially important for a very heavy Higgs boson, decaying into top quark pairs, where the form factors could be used for a differential description of the decay final state.

## 2.4. Electroweak Effects at the Top Threshold

*A. Hoang*

The proper treatment of electroweak effects plays an important role in high precision measurements at the  $t\bar{t}$  threshold. In the calculation of the total cross section, one can categorize electroweak effects into three classes.

- (a) "Hard" electroweak effects: This class includes electroweak effects related to the  $t\bar{t}$  production mechanism itself or factorizable corrections to various matching conditions of the effective theory that is used to describe the nonrelativistic QCD dynamics of the top pair. In general these corrections are modifications to the hard QCD matching conditions of the effective field theory operators. They can be determined by standard methods and are real numbers.
- (b) Electromagnetic effects: Electromagnetic effects are relevant for the luminosity spectrum of an  $e^+e^-$  initial state (beam energy spread, beamstrahlung, initial state radiation) and the  $t\bar{b}$  final state (modification to the Coulomb attraction, contributions to hard electroweak effects).
- (c) Effects related to the finite top quark lifetime: Apart from the top decay (into  $Wb$  for the Standard Model) this class also includes interference contributions with processes having the same final state ( $W^+W^-b\bar{b}$ ) but only one or even no top quark at intermediate stages. This class also accounts for interactions involving the top decay products ("non-factorizable" effects).

For processes involving highly energetic top quarks, where the momentum transfer typically involves scales much larger than  $\Gamma_t$ , the class (c) effects are small corrections. On the other hand, for the top threshold dynamics all three classes have to be accounted for at leading order, because the typical kinetic energy of the nonrelativistic top quarks is of the same order as the top quark width,

$$E_{\text{kin}} \sim m_t v^2 \sim m_t \alpha_s^2 \sim \Gamma_t \sim m_t \alpha_{\text{em}}. \quad (4)$$

The relation in Eq. (4) gives the power-counting that has to be employed to systematically account for electroweak effects within the nonrelativistic expansion:

$$v^2 \sim \alpha_s^2 \sim \alpha_{\text{em}}. \quad (5)$$

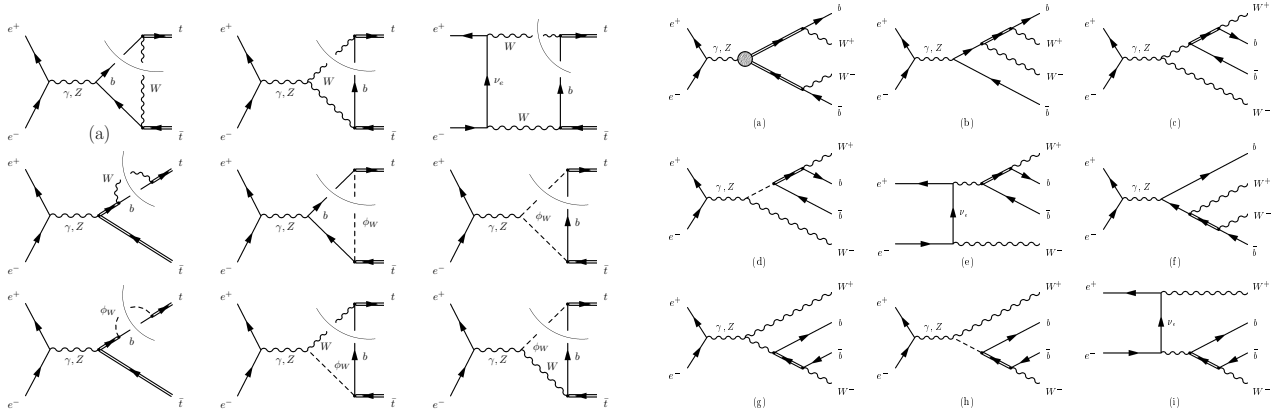


Figure 6: (a) Cuts in Standard Model diagrams contributing to absorptive parts in the matching conditions for the  $t\bar{t}$  effective theory currents. Within the effective theory the absorptive parts describe the interference of the diagrams shown in (b).

Several analyses concerning electroweak effects belonging to the various classes have been carried out in the past. However, no coherent and comprehensive treatment that systematically accounts for all these electroweak effects beyond leading order currently exists. In the following a brief status report is given concerning top threshold production in  $e^+e^-$  annihilation.

The leading order (LL) electroweak effects belonging to class (a) describe the production mechanisms of the nonrelativistic top quark pair in  $e^+e^-$  annihilation in the various possible spin and angular momentum states. Due to the power-counting, the one-loop hard electroweak corrections already contribute at next-to-next-to-leading order (NNLL) and involve the standard (real parts of the) one-loop electroweak corrections to the  $e^+e^- \rightarrow t\bar{t}$  process [36, 37]. There are also hard electroweak corrections that modify the QCD potentials [38], but due to gauge cancellations these corrections do not contribute at NNLL order. The dominant corrections caused by a exchange Higgs boson through a Yukawa potential can also be considered as a class (a) contribution.

The most important contribution belonging to the electromagnetic effects in class (b) is the luminosity spectrum that affects the c.m. energy available in the  $e^+e^-$  collision. While beamstrahlung and the beam energy spread are machine-dependent and will have to be measured experimentally, the initial state radiation component is calculable. The luminosity spectrum leads to sizeable smearing of the cross section and contributes at LL order. Electromagnetic effects also modify the QCD potential through photon exchange between the top pair and can lead to hard electroweak corrections belonging to class (a). In present analyses QED effects are only accounted for through the luminosity spectrum. In particular there is no coherent treatment of the calculable QED effects that systematically accounts for the effects of initial state radiation, the Coulomb corrections and the hard QED effects.

The leading order effect belonging to class (c) is the top decay width, which makes the perturbative treatment to the strong  $t\bar{t}$  dynamics at all possible [39, 40]. Within the nonrelativistic effective theory used to describe QCD effects the top quark width can be implemented through an imaginary mass shift in the top quark propagator

$$\frac{i}{k^0 - \frac{\mathbf{p}^2}{m_t} + \delta m_t + \frac{i}{2}\Gamma_t}, \quad (6)$$

where  $\delta m_t$  is related to the top quark mass definition that is used. This effect can be incorporated into the forward  $e^+e^- \rightarrow e^+e^-$  scattering amplitude results for stable top quarks by simply shifting the c.m. energy into the complex plane:  $\sqrt{s} \rightarrow \sqrt{s} + i\Gamma_t$ . Using the optical theorem one can obtain the total cross section. Beyond leading order the electroweak effects belonging to class (c) can be systematically incorporated into the effective theory by accounting for absorptive parts related to the top decay final states in the matching conditions [41] of the effective theory. This leads to well known effects such as the time dilatation correction [38], but can also account for interference contributions with processes where no top pairs are produced, but which have the same final state [41] (see Fig. 6). The gauge cancellation already mentioned for class (a) also applies here and leads to the cancellation of interactions among the

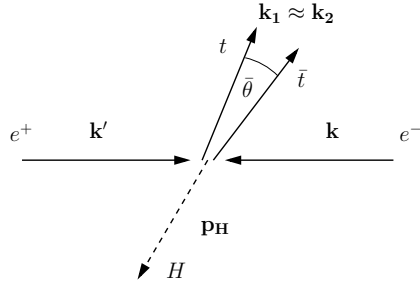


Figure 7: Typical constellation of momenta for the process  $e^+e^- \rightarrow t\bar{t}H$  in the large Higgs energy endpoint region.

top quarks and their decay products caused by ultrasoft gluons for the total cross section at NLL order [42, 43] and even at NNLL order [41]. In Ref. [41] it was also shown that within the nonrelativistic effective theory the imaginary matching conditions can lead to ultraviolet phase space divergences that require additional renormalization. A complete treatment of all the class (c) electroweak effect at NLL has not yet been achieved.

A crucial prediction of the Higgs mechanism is that the Higgs Yukawa coupling to quarks  $\lambda_q$  is related to the quark masses by  $m_q = \lambda_q V$ . At the  $e^+e^-$  Linear Collider the top quark Yukawa coupling can be measured from top quark pair production associated with a Higgs boson,  $e^+e^- \rightarrow t\bar{t}H$ . This process is particularly suited for a light Higgs boson since the cross section can then reach the 1-2 fb level. Assuming an experimental precision at the percent level, QCD and electroweak radiative corrections need to be accounted for in the theoretical predictions. The Born cross section was already determined some time ago in Refs. [44]. For the  $\mathcal{O}(\alpha_s)$  QCD one-loop corrections a number of references in various approximations exist [45, 46, 47]. On the other hand, the full set of one-loop electroweak corrections was obtained in Refs. [48, 49] and also in Refs. [50]. In Ref. [49] a detailed analysis of various differential distributions of the cross section  $\sigma(e^+e^- \rightarrow t\bar{t}H)$  can be found. For high energies these fixed order predictions are sufficient to reach the required theoretical precision.

In Ref. [51] the phase space region where the Higgs energy is large and the  $t\bar{t}$  pair becomes collinear to balance the large Higgs momentum was analyzed (see Fig. 7). It was found that since in this kinematic region the  $t\bar{t}$  invariant mass approaches  $2m_t$ , it is governed by nonrelativistic dynamics in analogy to the physics relevant for the  $t\bar{t}$  threshold. Thus, the usual fixed-order treatment breaks down and the nonrelativistic effective theory description known from the  $t\bar{t}$  threshold has to be applied. For high c.m. energies above about 700 GeV the large Higgs energy endpoint region is very small, and a usual fixed-order treatment is sufficient for the theoretical determination of the total cross section. However, for smaller c.m. energies (as available at the first phase of the ILC running), or for larger Higgs masses, the endpoint region increases with respect to the full available phase space and an effective theory treatment for the endpoint region becomes mandatory. In Ref. [51] a QCD endpoint analysis in the framework of the effective theory vNRQCD [52] was carried out. The results sum singular terms in the endpoint region  $\propto (\alpha_s/v)^n$  and  $(\alpha_s \ln v)^n$  at NLL order, where  $v$  is the c.m. velocity of the top quarks in the  $t\bar{t}$  c.m. frame. Typical results for the Higgs energy spectrum for small c.m. energies showing the fixed-order QCD predictions and the LL and NLL order nonrelativistic effective theory predictions in the large Higgs energy region are shown in Fig. 8. The vertical lines mark the Higgs energy where the top velocity  $v = 0.2$ , which roughly divides the regions where fixed-order and effective theory computations are valid. In Tab. III the impact of the summation of the Coulomb singularities and the logarithms of the top quark velocity in the endpoint region is analyzed numerically for various choices of the c.m. energy and the Higgs mass. For all cases the top quark mass  $m_t^{\text{1S}} = 180$  GeV is used and the other parameters are fixed as in Figs. 7. Here,  $\sigma(\text{Born})$  refers to the Born cross section and  $\sigma(\alpha_s)$  to the  $\mathcal{O}(\alpha_s)$  cross section in fixed-order perturbation theory using  $\mu = \sqrt{s}$  as the renormalization scale. The term  $\sigma(\text{NLL})$  refers to the sum of the  $\mathcal{O}(\alpha_s)$  fixed-order cross section for  $v > 0.2$  using  $\mu = \sqrt{s}v$  and the NLL nonrelativistic cross section for  $|v| < 0.2$  with the soft vNRQCD renormalization parameter  $\mu_S = 0.2m_t$ . The summation of endpoint singularities is particularly important for smaller c.m. energies, since it leads to an additional significant enhancement of the total cross section

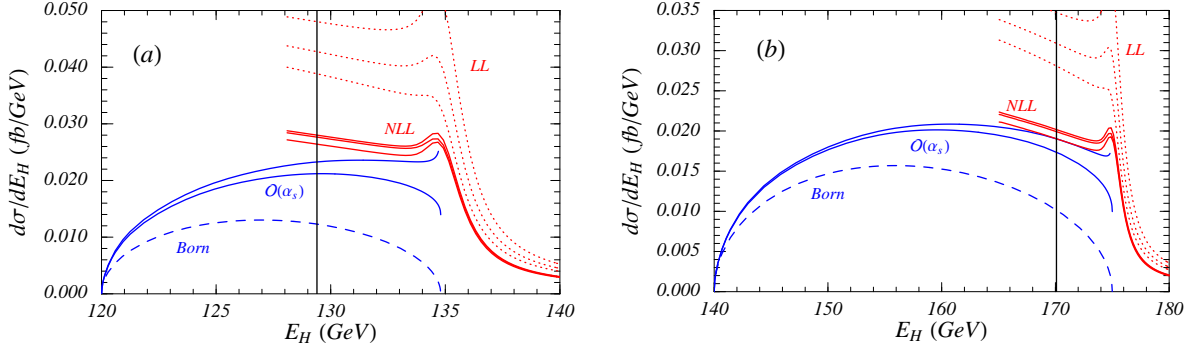


Figure 8: Higgs energy spectrum at LL (dotted lines) and NLL (solid lines) order in vNRQCD for the soft renormalization scales  $\mu_S = (0.1, 0.2, 0.4)m_t$  and at the Born level and at  $\mathcal{O}(\alpha_s)$  for  $\mu = \sqrt{s}, \sqrt{s}|v|$  for the parameters (a)  $\sqrt{s} = 500$  GeV,  $m_H = 120$  GeV and (b)  $\sqrt{s} = 550$  GeV,  $m_H = 140$  GeV. The top 1S mass has been set to  $m_t^{1S} = 180$  GeV and the other parameters are  $\Gamma_t = 1.55$  GeV,  $M_Z = 91.1876$  GeV,  $M_W = 80.423$  GeV,  $c_w = M_W/M_Z$  and  $\alpha^{-1} = 137.034$ .

$\sqrt{s}$ [GeV]	$m_H$ [GeV]	$\sigma(\text{Born})$ [fb]	$\sigma(\alpha_s)$ [fb]	$\sigma(\text{NLL})$ [fb]	$\frac{\sigma(\text{NLL})}{\sigma(\text{Born})}$	$\frac{\sigma(\text{NLL})}{\sigma(\alpha_s)}$
500	120	0.151	0.263	0.357(20)	2.362	1.359
550	120	0.984	1.251	1.342(37)	1.364	1.073
550	160	0.134	0.207	0.254(12)	1.902	1.226
600	120	1.691	1.939	2.005(30)	1.185	1.034
600	160	0.565	0.700	0.745(18)	1.319	1.065
700	120	2.348	2.454	2.485(13)	1.058	1.012
700	160	1.210	1.303	1.328(11)	1.098	1.020

Table III: Cross sections and K factors for  $\sigma_{\text{tot}}(e^+e^- \rightarrow t\bar{t}H)$  for various c.m. energies and Higgs masses and top quark mass  $m_t^{1S} = 180$  GeV.

in a region where the cross section is rather small. This enhancement could improve the prospects of top-Yukawa coupling measurements at the first phase of the ILC.

## 2.5. Towards a Precise Measurement of the Top Quark Yukawa Coupling at the ILC [53]

### A. Juste

The top quark Yukawa coupling ( $\lambda_t$ ) is the largest coupling of the Higgs boson to fermions. A precise measurement of it is very important since it may help unravel the secrets of the Electroweak Symmetry Breaking (EWSB) mechanism, in which the top quark could possibly play a key role. For  $m_h < 2m_t$ , a direct measurement of  $\lambda_t$  is possible via associated  $t\bar{t}h$  production, both at the LHC and a future ILC. At the LHC, the expected accuracy [54] is  $\delta\lambda_t/\lambda_t \sim 12 - 15\%$  for  $m_h \sim 120 - 200$  GeV, assuming an integrated luminosity of  $300 \text{ fb}^{-1}$ . Existing feasibility studies at the ILC [55] predict an accuracy of  $\delta\lambda_t/\lambda_t \sim 6 - 10\%$  for  $m_h \sim 120 - 190$  GeV, assuming  $\sqrt{s} = 800$  GeV and  $1000 \text{ fb}^{-1}$ . However, currently the baseline design for the ILC only contemplates a maximum center-of-mass energy of 500 GeV. Therefore, it is very relevant to explore the prospects of this measurement during the first phase of the ILC, especially in view of the limited accuracy expected at the LHC; for a number of years, the combination of results from the LHC and ILC will yield the most precise determination of  $\lambda_t$ .

A preliminary feasibility study at  $\sqrt{s} = 500$  GeV was performed in Ref. [56], which we briefly overview here. Indeed, the measurement of  $\lambda_t$  at  $\sqrt{s} = 500$  GeV is more challenging than at  $\sqrt{s} = 800$  GeV. On the one hand, the reduced phase-space leads to a large reduction in  $\sigma_{t\bar{t}h}$  (e.g.  $\sigma_{t\bar{t}h}^{\text{Born}} \simeq 0.16(2.5) \text{ fb}$  at  $\sqrt{s} = 500(800) \text{ GeV}$ , for

Table IV: Comparison of the Born and NLL  $\sigma_{t\bar{t}h}$  for different scenarios regarding radiative effects in the initial state.

(ISR,BS)	$\sigma_{t\bar{t}h}$ (fb) (Born)	$\sigma_{t\bar{t}h}$ (fb) (“NLL-improved”)	Enhancement factor
(off,off)	0.157(1)	0.357(2)	2.27
(off,on)	0.106(1)	0.252(3)	2.38
(on,on)	0.0735(8)	0.179(2)	2.44

$m_h = 120$  GeV). On the other hand, the cross section for many background processes is significantly increased. This analysis assumed  $m_h = 120$  GeV and focused on the  $t\bar{t}h \rightarrow (\ell\nu b)(j\bar{j}b)(b\bar{b})$  decay channel ( $BR \sim 30\%$ ). The dominant background is  $t\bar{t}j\bar{j}$ , followed by  $t\bar{t}Z$ , although other non-interfering backgrounds (e.g.  $W^+W^-$ ) were also considered. Signal and backgrounds were processed through a fast detector simulation. After basic preselection cuts, the signal efficiency was found to be  $\simeq 50\%$  and the  $S : B \simeq 1 : 100$ . In order to increase the sensitivity, a multivariate analysis using a Neural Network (NN) with 23 variables was performed. The final selection consisted on an optimized cut on the NN distribution. Assuming an integrated luminosity of  $1000 \text{ fb}^{-1}$ , the expected total numbers of signal and background events were 11 and 51, respectively, resulting in  $(\delta\lambda_t/\lambda_t)_{stat} \simeq 33\%$ . Based on previous experience [55], the addition of the fully hadronic decay channel was expected to ultimately lead to  $(\delta\lambda_t/\lambda_t)_{stat} \simeq 23\%$ . While this analysis is already rather sophisticated, significant improvements are expected from the usage of a more efficient  $b$ -tagging algorithm or a more optimal treatment of the kinematic information. In the next sections we discuss additional sources of improvement which are currently under investigation.

The precise measurement of  $\lambda_t$  requires accurate theoretical predictions for  $\sigma_{t\bar{t}h}$ . Currently, one-loop QCD and electroweak corrections are available. However, at  $\sqrt{s} = 500$  GeV and for  $m_h \geq 120$  GeV, the kinematic region where the  $t\bar{t}$  system is non-relativistic dominates. As discussed in Ref. [51], in this regime Coulomb singularities are important and need to be resummed within the framework of the vNRQCD effective theory, leading to large enhancements factors in the cross section relative to the Born level. At the ILC, because of ISR and beamstrahlung (BS), the event-by-event center-of-mass energy ( $\sqrt{\hat{s}}$ ) will be lower than the nominal one, thus bringing the  $t\bar{t}$  system deeper into the non-relativistic regime. In order to compute the expected  $\sigma_{t\bar{t}h}$  including these effects, the 11-fold Born differential cross section for  $e^+e^- \rightarrow t\bar{t}h \rightarrow W^+bW^-\bar{b}h$  was multiplied by a K-factor defined as  $K(E_h, \sqrt{\hat{s}}) = (d\sigma_{t\bar{t}h}^{NLL}/dE_h)/(d\sigma_{t\bar{t}h}^{Born}/dE_h)$ , where  $E_h$  stands for the Higgs boson energy in the  $e^+e^-$  rest-frame, and then folded with ISR and BS structure functions. The NLL differential cross section was kindly provided by the authors of Ref. [51]. Fig. 9 (left and center) compares the Born (for off-shell top quarks) and NLL differential cross sections for different values of  $\sqrt{\hat{s}}$ , assuming  $m_t^{\perp S} = 180$  GeV and  $m_h = 120$  GeV. The ratio of these two curves defines  $K(E_h, \sqrt{\hat{s}})$  and can be significantly larger than 1, especially for low values of  $\sqrt{\hat{s}}$ . Since the NLL prediction is only valid for  $E_h \leq E_h^{max}$  (where  $E_h^{max}$  effectively corresponds to a cut on the top quark velocity in the  $t\bar{t}$  rest-frame of  $\beta_t < 0.2$ ), we currently set  $K(E_h, \sqrt{\hat{s}}) = 1$  for  $E_h > E_h^{max}$ , although in practice, it should be possible to use  $K(E_h, \sqrt{\hat{s}}) = (d\sigma_{t\bar{t}h}^{O(\alpha_s)}/dE_h)/(d\sigma_{t\bar{t}h}^{Born}/dE_h)$ . Table IV compares the predicted Born and “NLL-improved”  $\sigma_{t\bar{t}h}$  for different scenarios, illustrating the large impact of radiative effects in the initial state. This underscores the importance of being able to predict these effects to the percent level. While the impact of ISR cannot be reduced, it might be possible to find an optimal operating point of the accelerator, as far as this measurement is concerned, in terms of BS and total integrated luminosity. Finally, it is found that, for  $m_h = 120$  GeV, resummation effects can increase  $\sigma_{t\bar{t}h}$  by a factor of  $\sim 2.4$  with respect to the Born cross section used in the previous feasibility study.

So far, all feasibility studies of this measurement have assumed unpolarized beams. Currently, the baseline design for the ILC only includes longitudinal electron beam polarization ( $|P_{e^-}| \simeq 0.8$ ). Positron beam polarization ( $|P_{e^+}| \simeq 0.6$ ) is considered as an option. The ratio of the polarized cross section (for arbitrary longitudinal beam polarization) ( $\sigma_{P_{e^-}P_{e^+}}$ ) to the unpolarized cross section ( $\sigma_0$ ) is given by  $\sigma_{P_{e^-}P_{e^+}}/\sigma_0 = (1 - P_{e^-}P_{e^+})(1 - P_{eff}A_{LR})$ , where  $P_{eff} = (P_{e^-} - P_{e^+})/(1 - P_{e^-}P_{e^+})$  denotes the “effective polarization” and  $A_{LR}$  is the “left-right asymmetry” of the process of interest [57]. Therefore, two potential enhancement factors can in principle be exploited: the first one requires having both beams polarized, the second one requires  $A_{LR} \neq 0$  and a judicious choice of the signs of  $P_{e^-}$  and

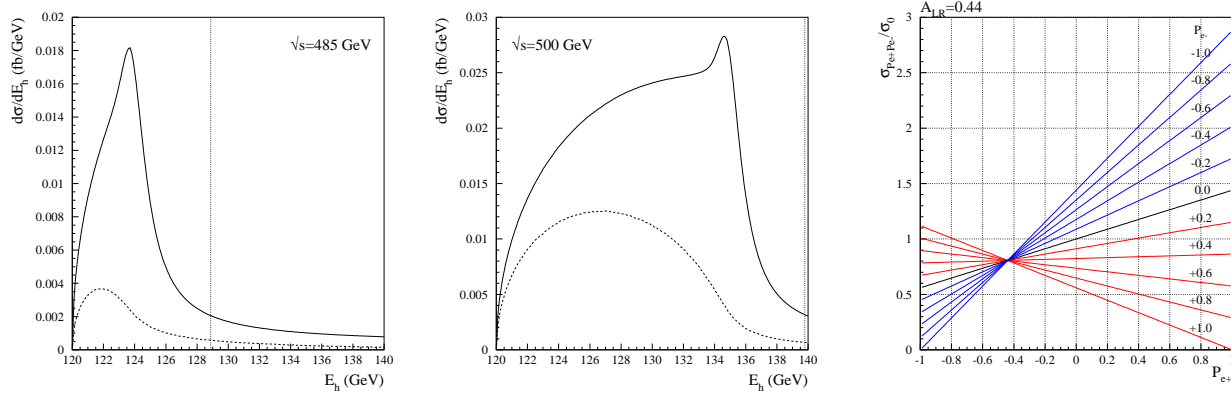


Figure 9: Left and center: comparison of the Born (dashed) and NLL (solid)  $d\sigma_{t\bar{t}h}/dE_h$  for different values of  $\sqrt{s}$ , assuming  $m_t^{1S} = 180$  GeV and  $m_h = 120$  GeV. The dotted line indicates the value of  $E_h^{max}$ . Right: ratio of polarized to unpolarized cross section for different values of  $(P_{e^-}, P_{e^+})$ .

$P_{e^+}$  in order to have  $P_{eff} A_{LR} < 0$ . In the case of SM  $t\bar{t}h$  production,  $A_{LR} \simeq 0.44$ , essentially independent of  $\sqrt{s}$  in the range  $\sim 0.5 - 1.0$  TeV. Assuming  $(A_{LR})_{SM}$ , Fig. 9 (right) shows the cross section enhancement factor as a function of  $P_{e^+}$ , for different values of  $P_{e^-}$ . The optimal (realistic) operating point would be  $(P_{e^-}, P_{e^+}) = (-0.8, +0.6)$ , achieving an increase in  $\sigma_{t\bar{t}h}$  by a factor of  $\simeq 2.1$  with respect to the unpolarized case. Unfortunately, this choice does not help reduce the dominant background, which is increased by a similar factor. Nevertheless, the net result is still an improvement in the statistical precision on  $\lambda_t$  by  $\sim 45\%$ , which would be an argument in favor of including positron polarization in the baseline design. For  $(P_{e^-}, P_{e^+}) = (-0.8, 0)$ , only a modest increase in  $\sigma_{t\bar{t}h}$  by a factor of  $\sim 1.3$  would be achieved. It is important to realize that, in order to choose the sign of  $P_{e^-}$  and  $P_{e^+}$ , it is necessary to know the sign of  $A_{LR}$ . Anomalous couplings in the  $t\bar{t}\gamma$  and  $t\bar{t}Z$  vertices could possibly lead to deviations in  $A_{LR}$  from the SM prediction. Unfortunately, due to the limited precision in the measurement of the  $t\bar{t}Z$  couplings [10], the LHC is not expected to provide any useful constraints on the sign of  $A_{LR}$ . Therefore, at the ILC the first step should be to perform measurements of the polarized  $\sigma_{t\bar{t}}$  in order to determine the sign of  $A_{LR}$ , and thus fix the signs of  $P_{e^-}$  and  $P_{e^+}$  (the magnitudes should be the largest possible). On the other hand, the measurement of  $\lambda_t$  requires a percent-level and model-independent determination of the  $t\bar{t}\gamma$  and  $t\bar{t}Z$  couplings, which typically benefits from changing the beam polarization. Therefore, it would be desirable to optimize the running strategy to maintain the largest possible  $\sigma_{t\bar{t}h}$ , needed for a precise measurement of  $\lambda_t$ , while meeting the precision goals for measurements of top quark couplings.

We have studied the prospects of a precise measurement of the top quark Yukawa coupling during the first phase of the ILC. Taking into consideration an existing feasibility study, and the additional enhancement factors to  $\sigma_{t\bar{t}h}$  discussed here, we anticipate a precision of  $(\delta\lambda_t/\lambda_t)_{stat} \sim 10\%$  for  $m_h = 120$  GeV, assuming  $\sqrt{s} = 500$  GeV and  $1000 \text{ fb}^{-1}$ .

## 2.6. The $t\bar{t}$ Threshold at an $e^+e^-$ Collider

Y. Kiyo

It is well known that QCD corrections to  $t\bar{t}$  production near threshold develop a Coulomb singularity. The structure of the cross section is

$$\sigma_{tot}(e^+e^- \rightarrow t\bar{t}) = \sigma_{Born} \left[ 1 + c^{(1)} \left( \frac{\alpha_s}{v} \right) + c^{(2)} \left( \frac{\alpha_s}{v} \right)^2 + c^{(3)} \left( \frac{\alpha_s}{v} \right)^3 + \dots + c^{(n)} \left( \frac{\alpha_s}{v} \right)^n + \dots \right], \quad (7)$$

where  $\sigma_{Born}$  is the Born cross section and  $v = \sqrt{1 - 4m_t^2/s}$  is the velocity of the top quarks. In (7) we have pulled out the Coulomb singularity  $(\alpha_s/v)^n$  explicitly so that the  $n$ th coefficient starts with  $\mathcal{O}(v^0)$ ,

$$c^{(n)} = c^{(n,0)} + c^{(n,1)} v + c^{(n,2)} v^2 + \dots \quad (8)$$

Near threshold the kinematics of the top quarks is non-relativistic and  $v \sim \alpha_s$  holds. To get a meaningful cross section we thus have to sum up the Coulomb singularities  $\sim \alpha_s/v \sim 1$ . The leading order (LO) cross section then contains the Coulomb singularities  $\sim (\alpha_s/v)^n$  to all orders of the coupling expansion,

$$\sigma_{tot}^{LO} = \sigma_{Born} \sum_{n=0} c^{(n,0)} \left( \frac{\alpha_s}{v} \right)^n \quad (9)$$

The  $c^{n,1}$  terms are suppressed by  $v$  compared with the LO and result in next-to-leading order (NLO) corrections. These terms are known since long. Next-to-next-to leading order (NNLO) calculations have been completed some time ago by several groups [58]. They sum up all the corrections of  $c^{(n,2)} v^2 (\alpha_s/v)^n$  to all orders  $n$ .

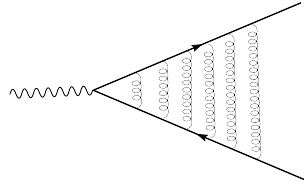


Figure 10: Typical QCD loop diagram which yields the Coulomb singularity  $\sim (\alpha_s/v)^n$ ,  $n =$  the number of gluon exchanges.

The Coulomb singularity originates from potential gluons, which have a typical momentum  $k^\mu \sim m_t(v^2, \vec{v})$ , exchanged between almost on-shell top and anti-top quarks in Fig. 10. For the kinematics of potential gluons, the corresponding propagator reduces to the Coulomb potential

$$\widetilde{V}_C = -\frac{4\pi C_F \alpha_s}{\mathbf{q}^2}, \quad (10)$$

where  $C_F = 4/3$ . In the gluon propagator, the energy component of  $q$  was set to zero because of the potential gluon's kinematics. Using this gluon propagator in place of normal gluon propagators in the figure, one may reproduce the  $c^{(i,0)}$  coefficients to all orders in Eq. 8. This procedure can be systematically extended to higher orders using effective field theory (EFT) techniques. The constructed effective field theories are versions of non-relativistic QCD called pNRQCD/vNRQCD [52]. We do not go into details of the EFT but summarize several features.

- The  $t\bar{t}$  pair at threshold is created by the production current  $\vec{J} = C_J [t\vec{\sigma}\bar{t}] + \dots$  in the EFT, where  $C_J$  is the Wilson coefficient of the corresponding current in the EFT, and the dots denote subleading operators.
- The produced top quark pair forms bound state resonances by exchanging potential gluons; the binding Coulomb potential is  $\widetilde{V}_0 = \mathcal{V}_0 \widetilde{V}_C(\mathbf{q})$ , where  $\mathcal{V}_0 = 1 + \mathcal{O}(\alpha_s)$  includes QCD corrections to the leading order Coulomb potential from loop diagrams.
- There are subdominant potentials, e.g.  $\widetilde{V}_1 = \mathcal{V}_1 g_s^2/|\mathbf{q}|$ , which have to be taken into account if one wants to go beyond the NLO cross section.
- A yet new type of corrections is known at next-to-next-to-next-to leading order (NNNLO), which is referred to as ultra-soft corrections because of the typical gluon momentum of  $k^0 \sim |\vec{k}| \sim mv^2$ .

An important point here is that the EFT scheme is a systematic way to sum up higher order corrections, and it makes practical calculations easier compared to those of full QCD. Currently complete NNLO total cross sections are known in both (semi-) analytical and numerical ways. The results are summarized in Ref.[58].

In the following we briefly survey recent attempts in going beyond NNLO and in resumming potentially large logarithms for the threshold cross section in the EFT framework.

In the EFT calculation of the  $t\bar{t}$  cross section, higher order QCD corrections enter through the higher order coefficients  $\mathcal{V}_i$  of potentials and through subdominant potentials, e.g.  $\tilde{V}_1(\mathbf{q})$ . Furthermore, there are corrections from ultra-soft gluons, starting to contribute at NNNLO. They cannot be written in form of potentials, as they include a noninstantaneous, dynamical propagation in time, while the potentials are all instantaneous. The first correction to  $\mathcal{V}_0$  is referred to as a Coulomb correction,

$$\mathcal{V}_0^{(n)} = 1 + \frac{\alpha_s}{4\pi} \left( \beta_0 L(q) + \frac{43}{9} \right) + \dots + \left( \frac{\alpha_s}{4\pi} \right)^n \cdot (\text{group factors, } L(q), \text{ etc.}), \quad (11)$$

where  $\beta_0 = 11 - (2/3)n_f$  is the coefficient of the QCD  $\beta$ -function,  $L(q) = \ln(\mu^2/\mathbf{q}^2)$ , and  $\mu$  is the QCD renormalization scale. The QCD corrections to all the coefficients can be found in Ref. [59] up to  $\mathcal{O}(\alpha_s^3)$ , except the third order constant term, so-called  $a_3$  in the literature. Using  $\tilde{V}_0^{(3)} = \mathcal{V}_0^{(3)} \tilde{V}_C$ , the Coulomb correction to the total cross section was computed in Ref. [60]. The other corrections to the  $t\bar{t}$  cross section at NNNLO due to subleading potentials and ultra-soft gluons are not known yet. In Fig. 11 we show the  $t\bar{t}$  threshold total cross section including the Coulomb

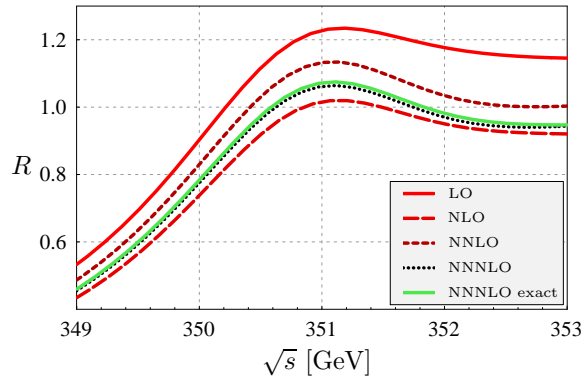


Figure 11: Normalized cross section  $R \equiv \sigma(e^+e^- \rightarrow t\bar{t})/\sigma(e^+e^- \rightarrow \mu^+\mu^-)$  in the threshold regime including the resummation of Coulomb corrections. Figure from [60].

corrections as calculated in [60]. The curves are obtained using analytical results of successive Coulomb corrections from LO to NNNLO, and the line denoted by "NNNLO exact" is obtained by numerically solving the Schrödinger equation using  $\mathcal{V}_0^{(3)}$  at NNNLO. The difference between NNNLO and "NNNLO exact" is yet of higher order as the numerical method contains rigid NNNLO plus additional contributions which come from iterations of the potential  $\tilde{V}_0$ . Studying the renormalization scale dependence of these predictions, the theoretical uncertainty for the NNNLO Coulomb corrections was estimated to be about 5% of the cross section. Although the full corrections at NNNLO are not known, the  $1S$  energy of  $t\bar{t}$  resonance, which corresponds to the peak position of the cross section, is known analytically at NNNLO from Refs. [59, 61]. The result shows that the uncertainty in the choice of the scale is small and the perturbative series for the  $1S$  energy is stabilized (see Ref. [62]).

In higher order calculations there appear potentially large logarithms of ratios of scales. In the threshold regime we have large logarithms of  $v$  in the coefficients  $c^{(n,i)}$ , arising from ratios of the largely different scales of the problem, namely the energy of the top quarks,  $E_t \sim mv^2$ , the momentum  $p \sim m_t v$  of almost on-shell top quarks, and the c.m. energy  $\sqrt{s} \sim 2m_t$ . The origin of these logarithms is related to UV divergences in the EFT. They can be resummed using renormalization group (RG) arguments [52, 63], resulting in RG improved cross section predictions,  $\sigma_{LL}, \sigma_{NLL}$ , etc. The RG improvement was extensively studied recently, and the next-next-leading-log (NNLL) cross section was calculated in Ref. [64] (apart from the NNLL running of a current for which the anomalous dimension is only fully known at NLL, see also Ref. [65]). The RG improved cross section then contains all terms of order

$\sum_{n,m} (\alpha_s/v)^n (\alpha_s \ln v)^m$ . The resummation of the logarithms leads to a reduction of the scale dependence of the normalization from 20% to about 6% (at NNLL), especially at energies around the  $1S$  peak, see Fig. 12 where the scale dependence of the fixed order (left panel) and RG improved (right panel) cross sections are shown for different orders.

The different studies discussed above strengthen our confidence that the estimate of the uncertainty of the top quark mass determination from [58],  $\Delta m_t < 100$  MeV, is realistic and will not be spoiled by uncalculated higher order corrections. There is even hope to believe that, if different approaches turn out to converge, the estimated error may shrink. For determinations of the top quark total width, the top Yukawa coupling  $y_t$  and the strong coupling constant from the threshold scan theoretical uncertainties are comparable to the expected experimental errors. An ultimate theoretical normalization error of at most 3% is desirable.

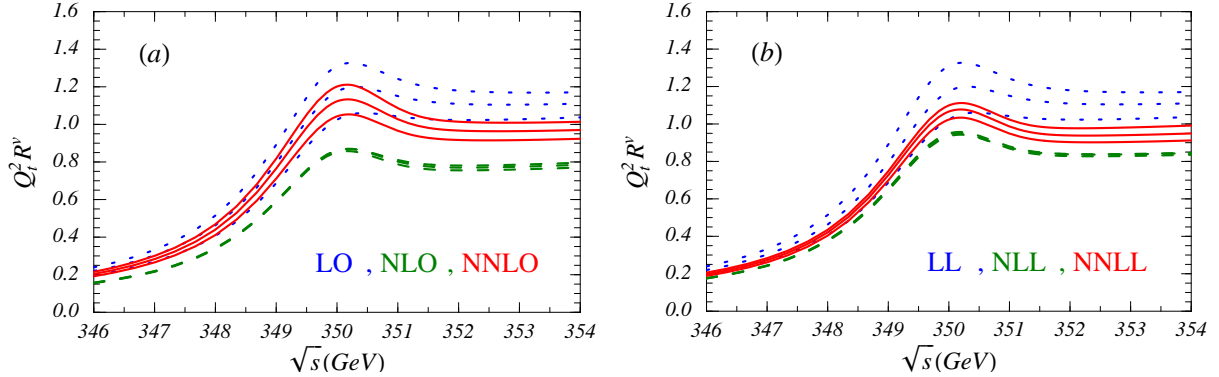


Figure 12: Scale dependence of the fixed order cross section (a) and the RG improved cross section predictions (b) in different orders. Each band of curves is obtained by varying the  $\nu$ NRQCD renormalization scale, choosing  $\nu = 0.15, 0.2, 0.3$ . Figures from [65].

## 2.7. Differential Distributions and Experimental Aspects of the $t\bar{t}$ Threshold Scan

*T. Teubner*

The most precise determination of the top quark mass will come from a dedicated threshold scan at  $\sqrt{s} \sim 2m_t$ . This is mainly a consequence of the fact that by performing a counting experiment of color singlet  $t\bar{t}$  pairs one can avoid most of the systematic uncertainties inherent in a kinematic reconstruction of the decay products of the colored quarks. These uncertainties, which are closely related to the problem of the mass definition, will ultimately limit the determination of  $m_t$  as done at the Tevatron and soon at the LHC. Detailed studies have shown that via a threshold scan, measurements with very small statistical and systematic errors will be possible at the ILC [2]. A multi-parameter fit for the top quark mass  $m_t$ , width  $\Gamma_t$ , the strong coupling  $\alpha_s$  and the top Yukawa coupling resulted in experimental errors of about  $\Delta m_t \sim 20$  MeV,  $\Delta \Gamma_t \sim 30$  MeV,  $\Delta \alpha_s \sim 0.0012$ , depending on details of the fit. (At threshold, the top Yukawa coupling can only be measured for a light Higgs and even then with less than 30% accuracy.) Such a precision will only be achieved if the accuracy of the theoretical predictions can match the experimental one, and recently a lot of effort has been invested in further improvements of the theory, see sections 2.4 and 2.6. Although most of the information in the fit will come from the precise  $t\bar{t}$  measurement of the total  $t\bar{t}$  cross section, differential distributions are needed for several reasons.

- Experimentally, cuts are needed to discriminate the signal from backgrounds, so the measured cross section can never be the fully inclusive total cross section.
- Distributions are required to build realistic (higher order) Monte Carlo generators for the signal process.

- Using additional observables beyond  $\sigma_{\text{tot}}$  adds information, helping to disentangle correlations between the parameters determined from a threshold scan, and increases the sensitivity to possible New Physics in top production and decay.

Differential distributions used so far are the top quark momentum distribution  $d\sigma/dp_t$  and the forward-backward asymmetry  $A_{\text{FB}}$  of the cross section, but theoretical studies exist also for the polarization of the top quarks. In the following we will briefly discuss these observables and their role in the threshold scan, and comment also on the issue of rescattering corrections.

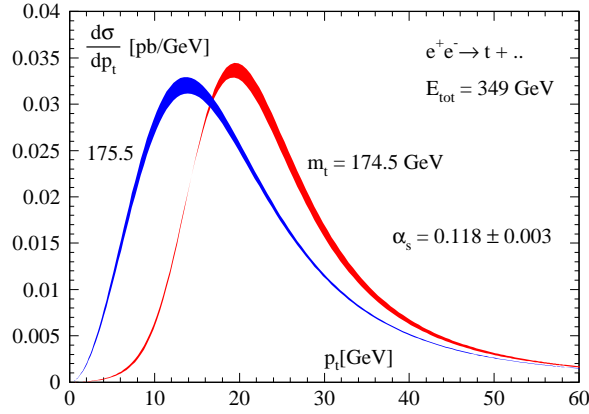


Figure 13: Top quark momentum distribution in the threshold regime.

The top quark momentum distribution  $d\sigma/dp_t$  is available in the framework of the next-to-next-to leading order (NNLO) calculations [66] (see also [67]). Close to threshold its form resembles a  $1S$  Coulomb-like wave function, becoming more symmetric well above threshold. Figure 13 shows  $d\sigma/dp_t$  at a fixed c.m. energy of 349 GeV for two different masses  $m_t = 174.5, 175.5$  GeV, where the width of the band is obtained by varying  $\alpha_s$  between 0.115 and 0.121. The peak position of  $d\sigma/dp_t$  is not much dependent on  $\alpha_s$  but is very sensitive to  $m_t$ , and a change of  $\alpha_s$  mainly affects the normalization of the distribution. This is in contrast to  $\sigma_{\text{tot}}$ , where  $m_t$  and  $\alpha_s$  are strongly correlated parameters when fitting theoretical predictions to (simulated) data.

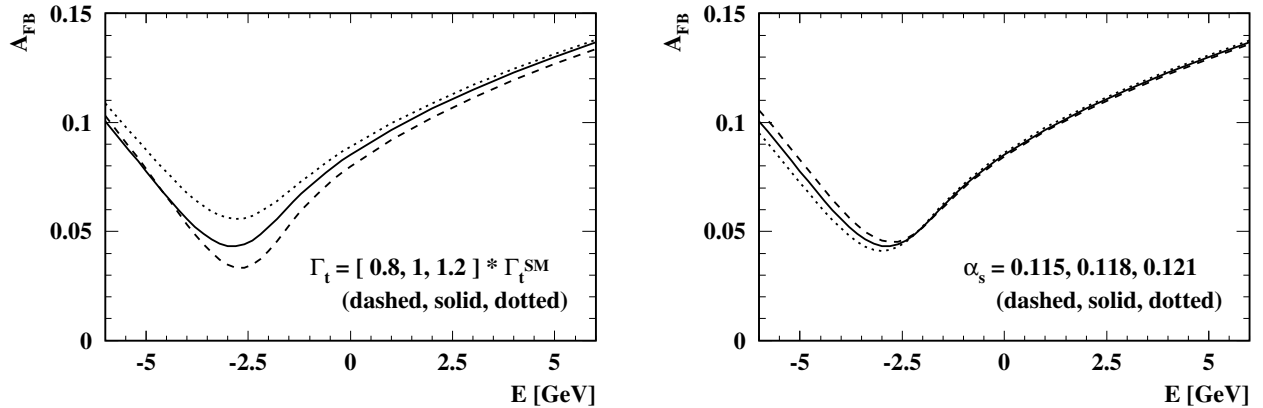


Figure 14: Dependence of the forward-backward asymmetry  $A_{\text{FB}}$  on the top quark width (left) and the strong coupling  $\alpha_s$  (right panel).

Interference of the leading vector current (through  $\gamma$  and  $Z$  exchange) with the suppressed axial vector contribution (from  $Z$  only) leads to a forward-backward asymmetry  $A_{\text{FB}}$ . The size of the asymmetry depends on how much the

corresponding  $S$  and  $P$  wave resonance contributions overlap and hence on the top quark width  $\Gamma_t$ , but less on  $\alpha_s$  (and  $m_t$ ), see Fig. 14.

As already demonstrated in experimental studies [2], the two observables  $d\sigma/dp_t$  and  $A_{FB}$  can be used together with  $\sigma_{tot}$  to make best use of the available information and to disentangle the correlations between the parameters  $m_t, \Gamma_t, \alpha_s, y_t$  in a multi-parameter fit. However, the latest theoretical developments such as NNNLO corrections, renormalization group improvement by summing large logarithms at NNLL order (see section 2.6) or the effect of EW corrections (see section 2.4) are dealing with the total cross section, whereas distributions are available at fixed NNLO only. This situation is quite common, as higher order corrections are increasingly difficult for differential cross sections, and not many distributions are known beyond NLO. Nevertheless, from a pragmatic point of view and for use in Monte Carlo, it is legitimate to use the best available prediction for the total cross section together with distributions available at lower order. By rescaling the distributions using the total cross section, their scale dependence will decrease and a consistent normalization will be ensured.

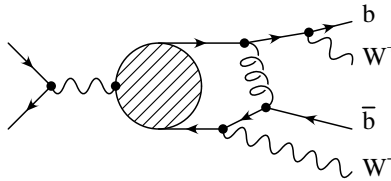


Figure 15: Feynman diagram responsible for rescattering corrections between the top and the  $\bar{b}$  from the  $\bar{t}$  decay.

All recent NNLO, NNNLO as well as the renormalization group improved calculations are not taking into account so-called rescattering corrections, i.e. interactions between the  $t, \bar{t}$  quarks and the  $b, \bar{b}$  quarks from the top decays, or between  $b$  and  $\bar{b}$ , see Fig. 16 for a typical Feynman diagram. However, such corrections were calculated numerically in [68, 69] to NLO accuracy. They are strongly suppressed (vanishing at NLO) in the inclusive  $\sigma_{tot}$  but generally important for distributions and typically of order 10%. They therefore should be included in a realistic Monte Carlo description.

In addition to differential distributions, also the top quark polarization has been studied in the threshold regime.[68, 69, 70] Predictions are available at NLO accuracy for all three polarization components, including rescattering corrections. Even for unpolarized  $e^+, e^-$  beams the top quarks are (longitudinally) polarized to 40%, and for the forseen beam polarization the top quarks will be highly polarized. Due to the short life-time the top polarization will be transmitted undisturbed to the decay  $b$ 's and  $W$ 's and allow very interesting studies. Making use of the polarization, observables can be defined which are sensitive to the top's electric dipole moment (probing CP-violation beyond the Standard Model) or to anomalous top couplings like  $V + A$  admixtures to the weak interaction. However, more realistic experimental studies are needed in order to fully explore the potential of polarization in the threshold regime.

#### *Experimental aspects of the threshold scan*<sup>1</sup>

Precision measurements from a  $t\bar{t}$  threshold scan require a very precise knowledge of both the average c.m. energy  $\langle\sqrt{s}\rangle$  and of the luminosity spectrum  $dL/d\sqrt{s}$ . [71] This is not an easy task, as the beam dynamics at a linear collider is not as constrained as it was e.g. at LEP, and only a single measurement of bunches before collision will be possible. The average c.m. energy can be determined by energy (up- and downstream) spectrometers in dedicated beam line inserts, discussed in Working Group 4 of the Snowmass Workshop. A possible problem here could be a bias between the spectrometer measurements and the collision c.m. energy. Another possibility to measure the beam energy is

<sup>1</sup>This section can only provide a brief review and the reader interested in more details is referred to the presentations of Stewart Boogert at this workshop.

the use of physics processes like  $Z$  pair production, or radiative return (through photon radiation) calibrated to the  $Z$  peak [72].

The luminosity spectrum is determined by (a) the beam spread, (b) beamstrahlung, and (c) initial state radiation (ISR). All three effects will lead to a smearing of the  $t\bar{t}$  threshold cross section, resulting in a significant reduction of the effective luminosity and hence the observed cross section,

$$\sigma^{\text{obs}}(\sqrt{s}) = \frac{1}{L_0} \int_0^1 L(x) \sigma(x\sqrt{s}) dx. \quad (12)$$

The influence of the three effects is demonstrated in Fig. 16. The beam spread will typically be  $\sim 0.1\%$  at the ILC and will cause comparably little smearing (though additional beam diagnostics may be required to measure and monitor the beam spread), but beamstrahlung and ISR are very important. The luminosity spectrum  $dL/d\sqrt{s}$  will lead to a systematic shift in the extracted top mass which must be well understood; otherwise it could become the dominant systematic error. In the past,  $t\bar{t}$  threshold studies were carried out under the assumption that the spectrum is basically known. However it has turned out that the precise determination of  $dL/d\sqrt{s}$  is a challenging task. The proposed method is to analyse the acollinearity of (large angle) Bhabha scattering events, which is sensitive to a momentum mismatch between the beams but insensitive to the absolute energy scale.[73] For this, the envisioned high resolution of the forward tracker will be very important to achieve the required accuracy.<sup>2</sup>

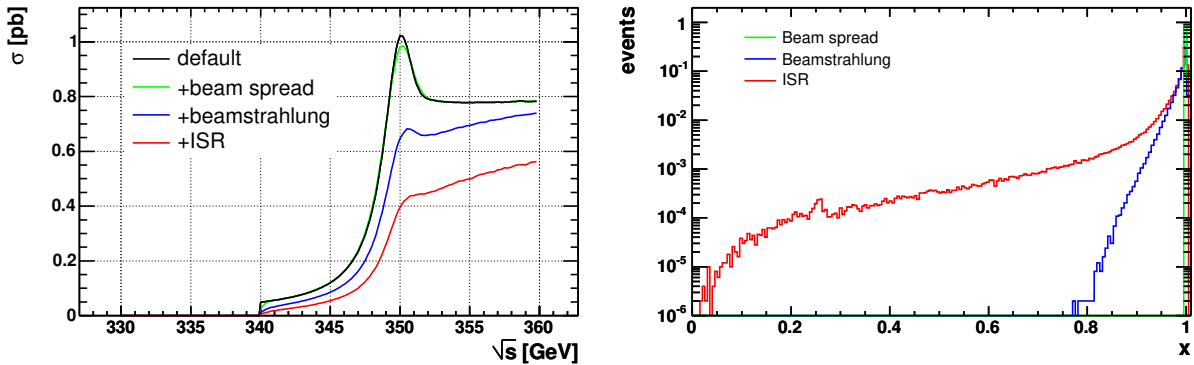


Figure 16: Left: Smearing of the theoretical  $t\bar{t}$  cross section ('default') by beam effects and initial state radiation. Right panel: Simulation of beam spread, beamstrahlung and ISR as distributions of  $x = \sqrt{s}/\sqrt{s_0}$  (where  $\sqrt{s_0}$  is the nominal c.m. energy of the machine).

In the simulation of the luminosity spectrum beamstrahlung is the main unknown. Integrated ILC accelerator simulations for these machine dependent effects are becoming available, including effects from the linac beam spread, the beam diagnostics and delivery system and the simulation of the collision dynamics using the package Guinea-pig. At this workshop Stewart Boogert presented first results of spectrum parametrizations (using the package CIRCE), based on new simulations from G. White for  $\sqrt{s} = 350$  GeV. The new parametrizations show variations from earlier results which were based on beam simulations at higher energies only. The parametrizations will be used as input in the simulation of the Bhabha scattering (based on the package BHWIDE) for the acollinearity analysis. These involved simulations are required to extract  $dL/d\sqrt{s}$  and to understand the uncertainties of the reconstructed spectrum. Only then can one quantify in physics analyses like the  $t\bar{t}$  threshold scan, to which extent the uncertainties in the luminosity spectrum affect the accuracy of the intended measurements like the top quark mass, width, etc.

The effects due to ISR are in principle machine independent and calculable to high precision in QED. Nevertheless, ISR effects complicate the measurement of beamstrahlung and accelerator energy spread, and one has to ensure that

<sup>2</sup>An additional complication is, that in Bhabha scattering ISR is not completely factorizable from final state radiation.

the precision of the theoretical formulae used in the Monte Carlo codes is sufficient. Similarly, the accuracy of differential distributions from programs used for the simulation of the wide angle Bhabha events must be assessed, and recent theoretical results [74] may have to be included.

The recent developments discussed here make it clear that much work remains to be done before the sophisticated analysis techniques for the  $t\bar{t}$  threshold scan are understood at the required level of accuracy. For a complete study, which should take into account the total cross section, distributions, full beam effects including asymmetric boosts and detector effects, a full Monte Carlo generator will be needed, and a project for this has been started at Snowmass. With a more detailed experimental study it will also be possible to optimize the scan strategy, i.e. how the available luminosity should be distributed between different energy scan points.

The analysis of beamstrahlung and its impact on the physics program at different energies will also be relevant for the optimization of the machine design. Concerning detectors, the demands of the top pair counting experiment are most probably not problematic for the existing detector designs. However, the requirements for Bhabha scattering and radiative  $Z$  return might set the requirements of the low angle tracking system and the electromagnetic calorimeter. Finally, it should also be noted, that the understanding of other physics processes like the  $WW$  or SUSY thresholds will largely benefit from the top case, and  $t\bar{t}$  at threshold should be regarded as the benchmark.

### 3. QCD EFFECTS IN ILC PHYSICS

#### 3.1. Precision QCD at the ILC: $e^+e^- \rightarrow 3$ Jets

*A. Gehrmann-De Ridder, T. Gehrmann, E.W.N. Glover*

The production of light quark-antiquark pairs in electron-positron annihilation gives rise to final states containing QCD jets. Depending on the amount of additional hard QCD radiation, one obtains final states with a certain number of jets: if only quark and antiquark are hard, two-jet final states are produced, one additional hard gluon yields a three-jet final state, two extra gluons or a secondary quark-antiquark pair can give rise to four-jet final states and so on. Studying these multi-jet final states, one can probe many aspects of perturbative QCD. Three-jet final states and related event shape observables were studied extensively at LEP in order to determine the strong coupling constant  $\alpha_s$ , which controls the probability of radiating a hard gluon in these events. The measurement of four-jet-type observables at LEP established the gauge group structure of QCD. Five-jet and higher multiplicities were sometimes considered in new physics searches, where QCD-induced processes form a theoretically calculable background.

The LEP measurements of three-jet observables are of a very high statistical precision. The extraction of  $\alpha_s$  from these data sets relies on a comparison of the data with theoretical predictions. Comparing the different sources of error in this extraction [75], one finds that the purely experimental error is negligible compared to the theoretical uncertainty. There are two sources of theoretical uncertainty: the theoretical description of the parton-to-hadron transition (hadronization uncertainty) and the theoretical calculation of parton-level jet production (perturbative or scale uncertainty). Although the precise size of the hadronization uncertainty is debatable and perhaps often underestimated, it is certainly appropriate to consider the scale uncertainty as the dominant source of theoretical error on the precise determination of  $\alpha_s$  from three-jet observables. This scale uncertainty arises from truncating the perturbative QCD expansion of jet observables at the next-to-leading order (NLO) and can be improved considerably by computing next-to-next-to-leading order (NNLO) corrections.

Given the planned luminosity of the ILC, one expects that this collider will deliver jet-production data of a statistical quality similar to LEP. An attractive perspective of such a measurement at the ILC would be to determine the evolution of  $\alpha_s$  over a wide energy range, which is potentially sensitive to new physics thresholds. Concerning uncertainties on such a determination, it is worthwhile to note that the hadronization corrections become less important at higher energies, thus leaving the scale uncertainty as dominant source of theoretical error. Experimental aspects of such measurements, especially issues related to the beam energy profile (which were irrelevant at LEP) were not studied up to now, and certainly deserve further attention.

In the recent past, many steps towards the NNLO calculation of  $e^+e^- \rightarrow 3$  jets have been accomplished (see [76] and references therein). Foremost, the relevant two-loop  $1 \rightarrow 3$  matrix elements are now available. One-loop corrections to  $1 \rightarrow 4$  matrix elements have been known for longer and form part of NLO calculations of  $e^+e^- \rightarrow 4$  jets. These NLO matrix elements naturally contribute to  $e^+e^- \rightarrow 3$  jets at NNLO if one of the partons involved becomes unresolved (soft or collinear). In this case, the infrared singular parts of the matrix elements need to be extracted and integrated over the phase space appropriate to the unresolved configuration to make the infrared pole structure explicit. As a final ingredient, the tree level  $1 \rightarrow 5$  processes also contribute to  $e^+e^- \rightarrow 3$  jets at NNLO. These contain double real radiation singularities corresponding to two partons becoming simultaneously soft and/or collinear. To compute the contributions from single unresolved radiation at one-loop and double real radiation at tree-level, one has to find subtraction terms which coincide with the full matrix elements in the unresolved limits and are still sufficiently simple to be integrated analytically in order to cancel their infrared pole structure with the two-loop virtual contributions. In the following, we present a new method, named antenna subtraction, to carry out NNLO calculations of jet observables and discuss its application to  $e^+e^- \rightarrow 3$  jets.

In electron-positron annihilation, an  $m$ -jet cross section at NLO is obtained by summing contributions from  $(m+1)$ -parton tree level and  $m$ -parton one-loop processes:

$$d\sigma_{NLO} = \int_{d\Phi_{m+1}} (d\sigma_{NLO}^R - d\sigma_{NLO}^S) + \left[ \int_{d\Phi_{m+1}} d\sigma_{NLO}^S + \int_{d\Phi_m} d\sigma_{NLO}^V \right].$$

The cross section  $d\sigma_{NLO}^R$  is the  $(m+1)$ -parton tree-level cross section, while  $d\sigma_{NLO}^V$  is the one-loop virtual correction to the  $m$ -parton Born cross section  $d\sigma^B$ . Both contain infrared singularities, which are explicit poles in  $1/\epsilon$  in  $d\sigma_{NLO}^V$ , while becoming explicit in  $d\sigma_{NLO}^R$  only after integration over the phase space. In general, this integration involves the (often iterative) definition of the jet observable, such that an analytic integration is not feasible (and also not appropriate). Instead, one would like to have a flexible method that can be easily adapted to different jet observables or jet definitions. Therefore, the infrared singularities of the real radiation contributions should be extracted using infrared subtraction terms. One introduces  $d\sigma_{NLO}^S$ , which is a counter-term for  $d\sigma_{NLO}^R$ , having the same unintegrated singular behavior as  $d\sigma_{NLO}^R$  in all appropriate limits. Their difference is free of divergences and can be integrated over the  $(m+1)$ -parton phase space numerically. The subtraction term  $d\sigma_{NLO}^S$  has to be integrated analytically over all singular regions of the  $(m+1)$ -parton phase space. The resulting cross section added to the virtual contribution yields an infrared finite result. Several methods for constructing NLO subtraction terms systematically were proposed in the literature [77, 78, 79, 80]. For some of these methods, extension to NNLO was discussed [82] and partly worked out. We focus on the antenna subtraction method [77, 78], which we extend to NNLO.

The basic idea of the antenna subtraction approach at NLO is to construct the subtraction term  $d\sigma_{NLO}^S$  from antenna functions. Each antenna function encapsulates all singular limits due to the emission of one unresolved parton between two color-connected hard partons (tree-level three-parton antenna function). This construction exploits the universal factorization of phase space and squared matrix elements in all unresolved limits, depicted in Figure 17. The individual antenna functions are obtained by normalizing three-parton tree-level matrix elements to the corresponding two-parton tree-level matrix elements.

At NNLO, the  $m$ -jet production is induced by final states containing up to  $(m+2)$  partons, including the one-loop virtual corrections to  $(m+1)$ -parton final states. As at NLO, one has to introduce subtraction terms for the  $(m+1)$ - and  $(m+2)$ -parton contributions. Schematically the NNLO  $m$ -jet cross section reads,

$$\begin{aligned} d\sigma_{NNLO} = & \int_{d\Phi_{m+2}} (d\sigma_{NNLO}^R - d\sigma_{NNLO}^S) + \int_{d\Phi_{m+2}} d\sigma_{NNLO}^S \\ & + \int_{d\Phi_{m+1}} (d\sigma_{NNLO}^{V,1} - d\sigma_{NNLO}^{VS,1}) + \int_{d\Phi_{m+1}} d\sigma_{NNLO}^{VS,1} \\ & + \int_{d\Phi_m} d\sigma_{NNLO}^{V,2}, \end{aligned}$$

where  $d\sigma_{NNLO}^S$  denotes the real radiation subtraction term coinciding with the  $(m+2)$ -parton tree level cross section  $d\sigma_{NNLO}^R$  in all singular limits [83]. Likewise,  $d\sigma_{NNLO}^{VS,1}$  is the one-loop virtual subtraction term coinciding with the

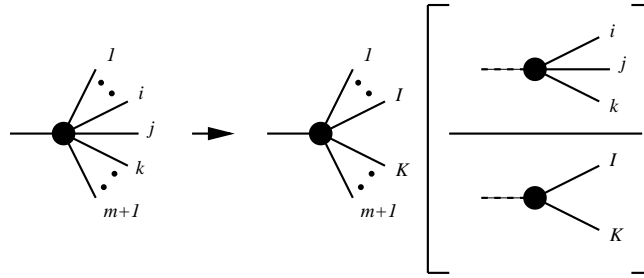


Figure 17: Illustration of NLO antenna factorisation representing the factorisation of both the squared matrix elements and the  $(m + 1)$ -particle phase space. The term in square brackets represents both the antenna function and the antenna phase space.

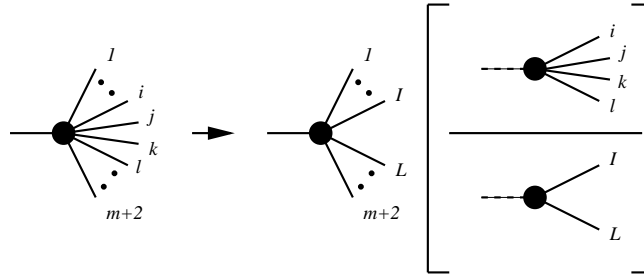


Figure 18: Illustration of NNLO antenna factorisation representing the factorisation of both the squared matrix elements and the  $(m + 2)$ -particle phase space when the unresolved particles are color connected. The term in square brackets represents both the antenna function and the antenna phase space.

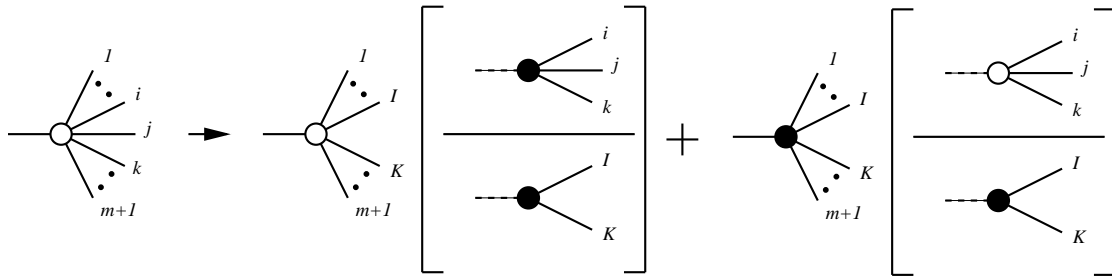


Figure 19: Illustration of NNLO antenna factorisation representing the factorisation of both the one-loop “squared” matrix elements (represented by the white blob) and the  $(m + 1)$ -particle phase space when the unresolved particles are color connected.

one-loop  $(m + 1)$ -parton cross section  $d\sigma_{NNLO}^{V,1}$  in all singular limits [84]. Finally, the two-loop correction to the  $m$ -parton cross section is denoted by  $d\sigma_{NNLO}^{V,2}$ .

Both types of NNLO subtraction terms can be constructed from antenna functions. In  $d\sigma_{NNLO}^S$ , we have to distinguish four different types of unresolved configurations: (a) One unresolved parton but the experimental observable selects only  $m$  jets; (b) Two color-connected unresolved partons (color-connected); (c) Two unresolved partons that are not color connected but share a common radiator (almost color-unconnected); (d) Two unresolved partons that are well separated from each other in the color chain (color-unconnected). Among those, configuration (a) is properly accounted for by a single tree-level three-parton antenna function like used already at NLO. Configuration (b) requires a tree-level four-parton antenna function (two unresolved partons emitted between a pair of hard partons) as shown in Figure 18, while (c) and (d) are accounted for by products of two tree-level three-parton antenna functions.

In single unresolved limits, the one-loop cross section  $d\sigma_{NNLO}^{V,1}$  is described by the sum of two terms [84]: a

tree-level splitting function times a one-loop cross section and a one-loop splitting function times a tree-level cross section. Consequently, the one-loop single unresolved subtraction term  $d\sigma_{NNLO}^{VS,1}$  is constructed from tree-level and one-loop three-parton antenna functions, as sketched in Figure 19. Several other terms in  $d\sigma_{NNLO}^{VS,1}$  cancel with the results from the integration of terms in the double real radiation subtraction term  $d\sigma_{NNLO}^S$  over the phase space appropriate to one of the unresolved partons, thus ensuring the cancellation of all explicit infrared poles in the difference  $d\sigma_{NNLO}^{V,1} - d\sigma_{NNLO}^{VS,1}$ .

Finally, all remaining terms in  $d\sigma_{NNLO}^S$  and  $d\sigma_{NNLO}^{VS,1}$  have to be integrated over the four-parton and three-parton antenna phase spaces. After integration, the infrared poles are rendered explicit and cancel with the infrared pole terms in the two-loop squared matrix element  $d\sigma_{NNLO}^{V,2}$ .

The subtraction terms  $d\sigma_{NLO}^S$ ,  $d\sigma_{NNLO}^S$  and  $d\sigma_{NNLO}^{VS,1}$  require three different types of antenna functions corresponding to the different pairs of hard partons forming the antenna: quark-antiquark, quark-gluon and gluon-gluon antenna functions. In the past [77, 78], NLO antenna functions were constructed by imposing definite properties in all single unresolved limits (two collinear limits and one soft limit for each antenna). This procedure turns out to be impractical at NNLO, where each antenna function must have definite behaviors in a large number of single and double unresolved limits. Instead, we derive these antenna functions in a systematic manner from physical matrix elements known to possess the correct limits. The quark-antiquark antenna functions can be obtained directly from the  $e^+e^- \rightarrow 2j$  real radiation corrections at NLO and NNLO [85]. For quark-gluon and gluon-gluon antenna functions, effective Lagrangians are used to obtain tree-level processes yielding a quark-gluon or gluon-gluon final state. The antenna functions are then obtained from the real radiation corrections to these processes. Quark-gluon antenna functions were derived [86] from the purely QCD (i.e. non-supersymmetric) NLO and NNLO corrections to the decay of a heavy neutralino into a massless gluino plus partons [87], while gluon-gluon antenna functions [88] result from the QCD corrections to Higgs boson decay into partons [89].

All tree-level three-parton and four-parton antenna functions and three-parton one-loop antenna functions are listed in [76], where we also provide their integrated forms, obtained using the phase space integration techniques described in [90].

In [76, 91] we derived the  $1/N^2$ -contribution to the NNLO corrections to  $e^+e^- \rightarrow 3$  jets. This color factor receives contributions from  $\gamma^* \rightarrow q\bar{q}ggg$  and  $\gamma^* \rightarrow q\bar{q}q\bar{q}g$  at tree-level [92],  $\gamma^* \rightarrow q\bar{q}gg$  and  $\gamma^* \rightarrow q\bar{q}q\bar{q}$  at one-loop [93] and  $\gamma^* \rightarrow q\bar{q}g$  at two-loops [94]. The four-parton and five-parton final states contain infrared singularities, which need to be extracted using the antenna subtraction formalism.

In this contribution, all gluons are effectively photon-like, and couple only to the quarks, but not to each other. Consequently, only quark-antiquark antenna functions appear in the construction of the subtraction terms.

Starting from the program **EERAD2** [77], which computes the four-jet production at NLO, we implemented the NNLO antenna subtraction method for the  $1/N^2$  color factor contribution to  $e^+e^- \rightarrow 3j$ . **EERAD2** already contains the five-parton and four-parton matrix elements relevant here, as well as the NLO-type subtraction terms.

The implementation contains three channels, classified by their partonic multiplicity: (a) in the five-parton channel, we integrate  $d\sigma_{NNLO}^R - d\sigma_{NNLO}^S$ ; (b) in the four-parton channel, we integrate  $d\sigma_{NNLO}^{V,1} - d\sigma_{NNLO}^{VS,1}$ ; (c) in the three-parton channel, we integrate  $d\sigma_{NNLO}^{V,2} + d\sigma_{NNLO}^S + d\sigma_{NNLO}^{VS,1}$ . The numerical integration over these channels is carried out by Monte Carlo methods.

By construction, the integrands in the four-parton and three-parton channel are free of explicit infrared poles. In the five-parton and four-parton channel, we tested the proper implementation of the subtraction by generating trajectories of phase space points approaching a given single or double unresolved limit. Along these trajectories, we observe that the antenna subtraction terms converge locally towards the physical matrix elements, and that the cancellations among individual contributions to the subtraction terms take place as expected. Moreover, we checked the correctness of the subtraction by introducing a lower cut (slicing parameter) on the phase space variables, and observing that our results are independent of this cut (provided it is chosen small enough). This behavior indicates that the subtraction terms ensure that the contribution of potentially singular regions of the final state phase space does not contribute to the numerical integrals, but is accounted for analytically.

As a final point, we noted in [76] that the infrared poles of the two-loop (including one-loop times one-loop)

correction to  $\gamma^* \rightarrow q\bar{q}g$  are cancelled in all color factors by a combination of integrated three-parton and four-parton antenna functions. This highly non-trivial cancellation clearly illustrates that the antenna functions derived here correctly approximate QCD matrix elements in all infrared singular limits at NNLO. They also outline the structure of infrared cancellations in  $e^+e^- \rightarrow 3j$  at NNLO, and indicate the structure of the subtraction terms in all color factors.

In this talk, we discussed the theoretical prerequisites for performing precision QCD studies on existing LEP data and at the ILC. In particular, the precise extraction of the strong coupling constant  $\alpha_s$  requires improved theoretical predictions to reduce the scale error inherent to calculations in perturbative QCD. At present, this extraction relies on the calculation of  $e^+e^- \rightarrow 3$  jets at NLO accuracy, and we reported on progress towards the NNLO calculation.

This calculation requires a new method for the subtraction of infrared singularities which we call antenna subtraction. We introduced subtraction terms for double real radiation at tree level and single real radiation at one loop based on antenna functions. These antenna functions describe the color-ordered radiation of unresolved partons between a pair of hard (radiator) partons. All antenna functions at NLO and NNLO can be derived systematically from physical matrix elements.

Using this method, we implemented the NNLO corrections to the subleading color contribution to  $e^+e^- \rightarrow 3$  jets into a flexible parton level event generator program, and are currently proceeding with the implementation [95] of the full set of color factors relevant to the NNLO corrections to  $e^+e^- \rightarrow 3$  jets.

### 3.2. Study of $V_L V_L \rightarrow t\bar{t}$ at the ILC Including $\mathcal{O}(\alpha_s^2)$ Corrections [96]

*S. Godfrey*

Understanding the mechanism of electroweak symmetry breaking (EWSB) is a primary goal of the LHC and ILC [54]. While much effort has been devoted to the weakly interacting weak sector scenario the strongly interacting weak sector (SIWS) remains a possibility. Because the  $t$ -quark mass is the same order of magnitude as the scale of EWSB it has long been suspected that  $t$ -quark properties may provide hints about the nature of EWSB and the subprocess  $V_L V_L \rightarrow t\bar{t}$  has been suggested as a probe. While  $V_L V_L \rightarrow t\bar{t}$  can be studied at both hadron colliders and  $e^+e^-$  colliders the overwhelming QCD backgrounds will likely make it impossible to study the  $V_L V_L \rightarrow t\bar{t}$  subprocess at the LHC [97]. In contrast, the ILC offers a much cleaner environment. But to be able to attach meaning to precision measurements it is necessary to understand radiative corrections, both electroweak and QCD. Here we show  $\mathcal{O}(\alpha_s)$  corrections to the tree level electroweak  $V_L V_L \rightarrow t\bar{t}$  process in the SM at the ILC. Due to space limitations we point the interested reader to Ref. [98] for a more detailed account and a more complete set of references.

We are interested in the subprocesses  $VV \rightarrow t\bar{t}$  which occur in the processes  $e^+e^- \rightarrow \ell_1 \ell_2 + VV \rightarrow \ell_1 \ell_2 + t\bar{t}$  where  $\ell_1 \ell_2$  is  $\nu\bar{\nu}$  for the  $W^+W^- \rightarrow t\bar{t}$  subprocess and  $e^+e^-$  for the  $ZZ \rightarrow t\bar{t}$  subprocess. The vector bosons are treated as partons inside the  $e^+$  and  $e^-$  using the effective boson approximation [99, 100]. The total cross section is then obtained by integrating the  $W$  (of  $Z$ ) luminosities with the subprocess cross section [101].

The  $\mathcal{O}(\alpha_s)$  corrections for the processes  $W^+W^- \rightarrow t\bar{t}$   $ZZ \rightarrow t\bar{t}$  are calculated using the FeynArts, FormCalc and LoopTools packages [102]. The QCD corrections to  $W^+W^- \rightarrow t\bar{t}$  are shown in Fig. 20 (left side). The infrared singularity in the vertex corrections are cancelled by the soft contributions from the process  $W^+W^- \rightarrow t\bar{t}g$  which are shown in Fig. 20 (right side). We regulate the IR-singularity by introducing a gluon mass which is equivalent to standard dimensional regularization for processes with no triple gluon vertex present. This approach has the additional benefit that varying the value of the gluon mass acts as a check of the numerical cancellations between the different contributions.

We include in our results the kinematic cuts  $m_{t\bar{t}} > 400$  GeV and  $p_T^{t,\bar{t}} > 10$  GeV. Since the longitudinal scattering cross section is much larger than the  $TT$  and  $TL$  cases and it is the longitudinal gauge boson processes which corresponds to the Goldstone bosons of the theory we will henceforth only include results for  $V_L V_L$  scattering.

The QCD corrections to longitudinal scattering are often presented as a K-factor, normally defined as the ratio of the NLO to LO cross sections. Because the  $\mathcal{O}(\alpha_s)$  QCD corrections we calculated are LO corrections to a tree level electroweak result we take the K-factor to be the ratio of the cross section with the  $\mathcal{O}(\alpha_s)$  QCD corrections and

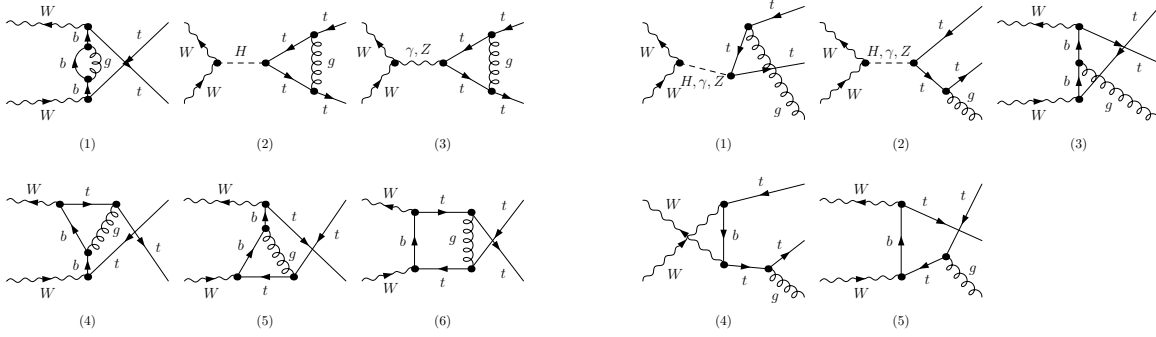


Figure 20:  $\mathcal{O}(\alpha_s)$  QCD corrections to  $W^+W^- \rightarrow t\bar{t}$ . (a) Virtual QCD contributions to  $W^+W^- \rightarrow t\bar{t}$ . (b) Feynman diagrams for  $W^+W^- \rightarrow t\bar{t} + g$ .

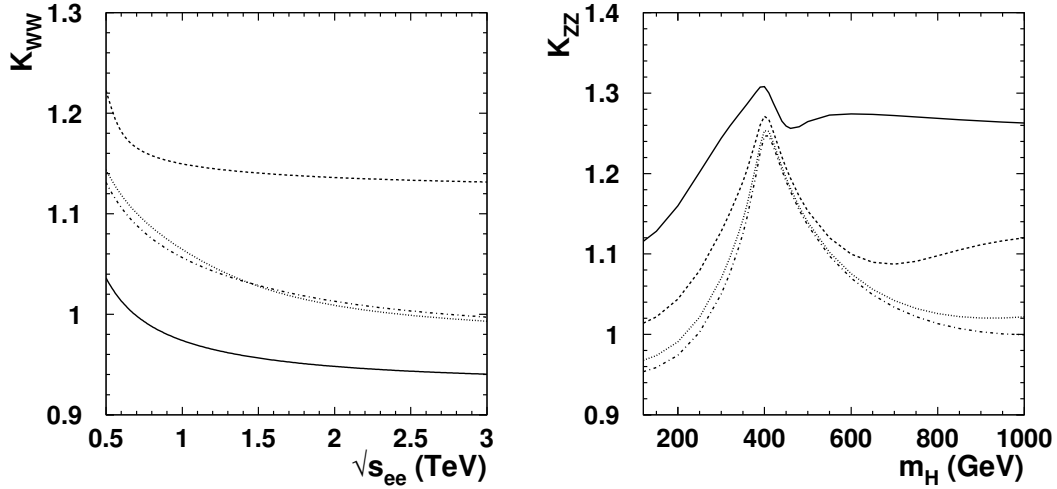


Figure 21: (left side) The K-factors as a function of  $\sqrt{s_{e^+e^-}}$  for  $e^+e^- \rightarrow \nu\bar{\nu}t\bar{t}$  (via  $W_L^+W_L^-$  fusion). The solid line is for  $M_H = 120$  GeV, the dashed line for  $M_H = 500$  GeV, the dotted line for  $M_H = 1$  TeV, and the dot-dashed line for  $M_H = \infty$  (LET). (right side) The K-factor as a function of  $M_H$  for  $e^+e^- \rightarrow \nu\bar{\nu}t\bar{t}$  (via  $W_L^+W_L^-$  fusion). The solid line is for  $\sqrt{s_{e^+e^-}} = 500$  GeV, the dashed line for  $\sqrt{s_{e^+e^-}} = 1$  TeV, the dotted line for  $\sqrt{s_{e^+e^-}} = 2$  TeV, and the dot-dashed line for  $\sqrt{s_{e^+e^-}} = 3$  TeV. See text for an explanation of the K-factor.

the tree level electroweak cross sections. The K-factors for  $\sigma(e^+e^- \rightarrow \nu\bar{\nu}t\bar{t})$  which goes via  $W_L^+W_L^-$  fusion and for  $\sigma(e^+e^- \rightarrow e^+e^-t\bar{t})$  is shown in Fig. 21 (left side) as a function of  $\sqrt{s_{e^+e^-}}$ . The  $\mathcal{O}(\alpha_s)$  QCD corrections are largest for  $M_H = 500$  GeV with K-factors ranging from over 1.2 for  $\sqrt{s_{e^+e^-}} = 500$  GeV to 1.15 for  $\sqrt{s_{e^+e^-}} = 1$  TeV. The corrections decrease as  $\sqrt{s_{e^+e^-}}$  increases. The variation of the K-factor with  $M_H$  is shown in Fig. 21 (right side). The fact that the K-factor is largest for  $M_H = 500$  GeV in Fig. 21 (left side) and that it peaks at  $M_H \simeq 400$  GeV in Fig. 21 (right side) is a threshold effect which is an artifact of the kinematic cut we imposed on the  $t\bar{t}$  invariant mass. The important point is that the QCD corrections are not insignificant compared to the effects we might wish to study such as top Yukawa couplings or anomalous  $VVt\bar{t}$  couplings.

### 3.3. QCD at a Photon Collider [103]

Z. Sullivan

A terascale photon collider will provide a unique opportunity to understand the resolved hadronic structure of light beyond a few GeV. This structure completely dominates the QCD cross section if the invariant mass of hadronic final

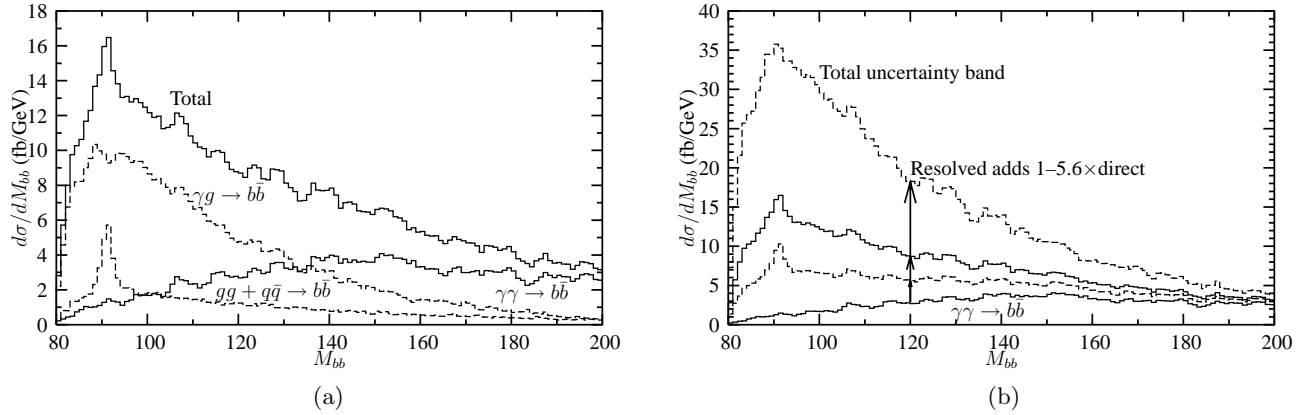


Figure 22: (a) Breakdown of contributions to the  $bb$ -dijet cross section vs. dijet invariant mass  $M_{bb}$ . (b) Range of theoretical predictions for  $bb$ -dijet cross section vs. dijet invariant mass  $M_{bb}$ .

state particles is less than  $\sim W_{\max}/3$ . This is clear from Fig. 22(a), where we see the cross section for  $bb$  production as a function of invariant mass  $M_{bb}$ . The first calculation of the uncertainty in this cross section is presented in detail in the Proceedings of this workshop [103]. The result, the dashed band surrounding the upper solid curve in Fig. 22(b), is that the cross section cannot be predicted to better than a factor of 5. There is no way to improve this prediction without measuring the gluon, charm, and bottom parton distributions for the photon *in situ* at this collider.

Loosening the cuts used for Fig. 22(a) will provide an extremely clean sample of events with a gluon in the initial state. Hence, the gluon structure should be quickly well-measured. The peak near 90 GeV is from a  $Z$  resonance, for which 40% of the events come from a  $c\bar{c}$  initial state. Therefore, a clean extraction of the charm structure can be made by reconstructing the  $Z$  peak in multiple channels (particularly  $Z \rightarrow \mu^+\mu^-$ ). Finally, the long resolved-resolved tail above the  $Z$  peak is almost entirely due to  $bb + \bar{b}\bar{b} + b\bar{b}$  collisions. Therefore, given enough data, even the bottom structure may be accessible.

The study [103] focused on a photon-photon collider, but another option being considered is a photon-electron collider. In general, it is more difficult to cleanly extract the gluon PDF in a  $\gamma$ - $e$  collision than a  $\gamma$ - $\gamma$  collision, because the cross section at high invariant mass ( $> 20$  GeV) is smaller, the decay products tend to be boosted more forward into less-well instrumented regions of the detector, and an additional deconvolution must be performed to remove the effect of extracting an almost-real photon from the electron. Nevertheless, this option should be examined in more detail as it may be simpler to construct a  $\gamma$ - $e$  collider.

## 4. NEW PHYSICS EFFECTS ON TOP QUARK PROPERTIES

### 4.1. Top Compositeness at Colliders

*K. Agashe*

Consider the Randall-Sundrum (RS1) model [104] which is a compact slice of  $AdS_5$ ,

$$ds^2 = e^{-2k|\theta|r_c} \eta^{\mu\nu} dx_\mu dx_\nu + r_c^2 d\theta^2, \quad -\pi \leq \theta \leq \pi, \quad (13)$$

where  $k$  is the curvature scale and the extra-dimensional interval is realized as an orbifolded circle of radius  $r_c$ . The two orbifold fixed points,  $\theta = 0, \pi$ , correspond to the “UV” (or “Planck”) and “IR” (or “TeV”) branes respectively. In warped spacetimes the relationship between 5D mass scales and 4D mass scales (in an effective 4D description) depends on location in the extra dimension through the warp factor,  $e^{-k|\theta|r_c}$ . This allows large 4D mass hierarchies to naturally arise without large hierarchies in the defining 5D theory, whose mass parameters are taken to be of order

the observed Planck scale,  $M_{Pl} \sim 10^{18}$  GeV. For example, the 4D massless graviton mode is localized near the UV brane while the Higgs sector is taken to be localized on the IR brane. In the 4D effective theory one then finds

$$\text{Weak Scale} \sim M_{Pl} e^{-k\pi r_c}. \quad (14)$$

A modestly large radius, i.e.,  $k\pi r_c \sim \log(M_{Pl}/\text{TeV}) \sim 30$ , can then accommodate a TeV-size weak scale. Kaluza-Klein (KK) graviton resonances have masses  $m \sim k e^{-k\pi r_c}$ . These masses are at the TeV-scale, since their wave functions are also localized near the IR brane.

In the original RS1 model, it was assumed that the entire SM was localized on the TeV brane, and that only gravity propagated in the full 5D space. Thus, the effective UV cut-off for gauge and fermion fields and hence the scale suppressing higher-dimensional operators is at a TeV, the same scale which sets the Higgs sector. However, bounds from electroweak precision tests (EWPT) on this cut-off are approximately 5-10 TeV, while those from flavor changing neutral currents (FCNCs) such as  $K - \bar{K}$  mixing are around 1000 TeV. Stabilizing the electroweak scale thus requires fine-tuning; even though RS1 explains the big hierarchy between the Planck and electroweak scales, it has a “little” hierarchy problem between the weak scale and the TeV scale cut-off.

An attractive solution to this problem is to allow the SM gauge [105] and fermion [106, 107] fields to propagate in the extra dimensional bulk. We first explain how bulk fermions enable us to evade flavor constraints. The localization of the wavefunction of the massless chiral mode is controlled by the 5d mass term for each fermion, which in units of  $k$  is denoted by the  $c$ -parameter. In the warped scenario, for  $c > 1/2$  ( $c < 1/2$ ) the zero mode is localized near the Planck (TeV) brane, whereas for  $c = 1/2$ , the wave function is flat. We therefore choose  $c > 1/2$  for light fermions so that the effective UV cut-off at the location of the light fermions is much greater than a TeV, suppressing dangerous FCNCs. This naturally results in a small 4D Yukawa coupling to the Higgs on the TeV brane without any hierarchies in the fundamental 5D Yukawa couplings [106, 107, 108]. Similarly, we choose  $c \ll 1/2$  for the top quark to obtain an  $O(1)$  Yukawa coupling. We can also show that in this scenario with bulk gauge fields high-scale unification of gauge couplings can be accommodated.

Since gauge fields are also in the bulk, their excited KK modes induce additional effects in flavor physics and in EWPT, which are calculable in the 5D effective field theory. For example, the couplings of KK modes to light fermions are flavor-dependent, giving FCNCs. However, this flavor dependence is small. KK modes, just like the Higgs, are localized near the TeV brane, whereas the light fermions are near the Planck brane. The FCNCs are therefore proportional to the Yukawa couplings, resulting in a suppression of flavor violation. This scenario has an analog of the Glashow-Iliopoulos-Maiani (GIM) mechanism of the SM, resulting in the suppression of the calculable FCNCs [107, 108].

Early studies showed that the corrections to EWPT from gauge KK modes are too large, unless the KK mass is greater than 10 TeV [109]. Such a large KK scale results in a little hierarchy problem between the weak and KK scales. The localization of the light fermions near the Planck brane reduces the contribution of gauge KK modes to two observables – the  $S$  parameter and 4-fermion operators, but the observable called the  $T$  parameter still gives stringent constraints.

In reference [110], it was shown that this problem can be avoided by extending the electroweak gauge group in the bulk to  $SU(2)_L \times SU(2)_R \times U(1)_{B-L}$ . Such an extension provides a custodial isospin symmetry to protect the  $T$  parameter from large corrections. Thus, KK masses as low as 3 TeV are allowed by oblique EW data, significantly ameliorating the little hierarchy problem.

We now consider the top and bottom quarks. It is clear that we prefer  $c \ll 1/2$  for  $t_L$  to obtain a top Yukawa coupling of  $O(1)$  without too large a 5D Yukawa coupling, but this implies a large shift in coupling of  $b_L$  to the  $Z$ -boson unless the KK scale is larger than a TeV. This shift occurs due to the large coupling of  $b_L$  to the KK  $Z$  modes, which mix with the zero-mode  $Z$  via the Higgs vev [110]:

$$\left. \frac{\delta(g_Z^{tR})}{g_Z^{tR}} \right|_{\text{KK gauge}} \approx \frac{m_Z^2}{(0.41 m_{KK})^2} \frac{1 - 2c_R}{3 - 2c_R} \left( -\frac{k\pi r_c}{2} + \frac{5 - 2c_R}{4(3 - 2c_R)} \right). \quad (15)$$

Here,  $m_{KK} \approx 2.45 k e^{-k\pi r_c}$  is defined to be the mass of the lightest gauge KK mode. Thus, there is a tension between obtaining the top Yukawa and not shifting the coupling of  $b_L$  to  $Z$ . As a compromise, KK masses  $\sim 5$  TeV

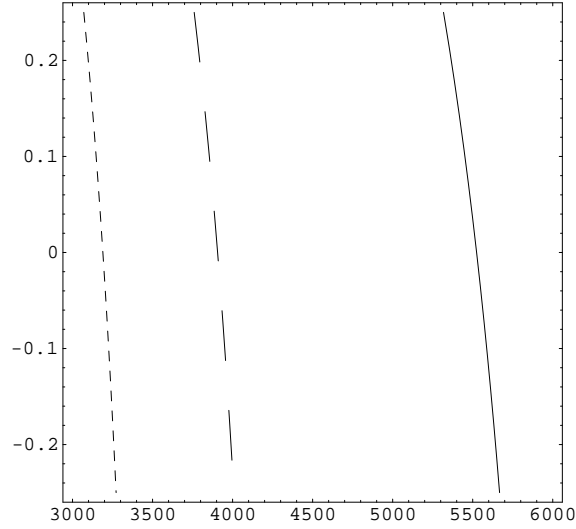


Figure 23: Shift in the coupling of  $t_R$  to  $Z$  as a function of KK mass in GeV on horizontal axis and  $c_R$  on vertical axis for the choice  $c_L = 0.4$ . The solid, long-dashed and short-dashed lines correspond to shifts of 5%, 10% and 15%, respectively.

are consistent with a shift in  $g_Z^{b_L}$  of approximately 0.25% for  $c_L \sim 0.4$ . The  $t_R$  must therefore be localized near the TeV brane:  $c_R \lesssim 0$ . Such a profile for  $t_R$  leads to sizable shift in its coupling to the  $Z$  via exchange of KK  $Z$ -bosons, and also via KK  $t_L$  modes. The additional contribution from KK  $t_L$  exchange is due to zero-mode  $t_R$  mixing with KK  $t_L$  via a Higgs vev which then couples to the  $Z$ , giving the shift

$$\left. \frac{\delta(g_Z^{t_R})}{g_Z^{t_R}} \right|_{\text{KK fermion}} \approx \sum_n \frac{1/2}{-2/3 \sin^2 \theta_W} \left( \frac{m_t \sqrt{1/2 - c_L}}{m_{t_L^{(n)}}} \right)^2. \quad (16)$$

Here  $m_t \sqrt{1/2 - c_L}$  is the mass term coupling zero-mode and KK top quarks, and the KK  $t_L$  masses are given by  $m_{t_L^{(n)}} \approx \pi k e^{-k\pi r_c} (n - c_L/2) \approx 0.78 m_{KK} (n - c_L/2)$ .

The total shift in the coupling of  $t_R$  is plotted in Fig. 23. As seen in the figure, we obtain an 10% shift for KK masses of a few TeV. Smaller KK masses are not allowed by EWPT, and larger masses lead to large fine-tuning. Observability of an effect of this size might be difficult at the LHC since the sensitivity of the LHC is only at the 20% level for a shift in the axial coupling of the top quark to the  $Z$ . It should be possible at the ILC, which has sensitivity at the few percent level for shifts in both axial and vector couplings of the top quark to  $Z$  [10]. There are similar shifts in couplings of Higgs to  $W/Z$  due to its profile being localized near TeV brane just like for  $t_R$ .

Finally, an intriguing aspect is that via the AdS/CFT correspondence [111], such a scenario is conjectured to be dual to a purely 4D theory with a composite Higgs boson [112], with the light fermions being elementary and  $t_R$  being composite. This provides an intuitive understanding for the large shifts in the couplings of  $t_R$  and Higgs to  $Z$ . Hence, these signals might be valid for general composite Higgs models as well.

## 4.2. Top quark properties in Little Higgs Models [114]

*C.F. Berger, M. Perelstein, F. Petriello*

In this section, we study the corrections to the top quark properties in “Little Higgs” models of electroweak symmetry breaking [113], and compare the expected deviations from the SM predictions with expected sensitivities of experiments at the LHC and the ILC. In the Little Higgs models, electroweak symmetry is driven by the radiative effects from the top sector, including the SM-like top and its heavy counterpart, a TeV-scale “heavy top”  $T$ . Probing this structure experimentally is quite difficult. While the LHC should be able to discover the  $T$  quark, its potential for studying its couplings is limited [115, 116]. Direct production of the  $T$  will likely be beyond the kinematic reach

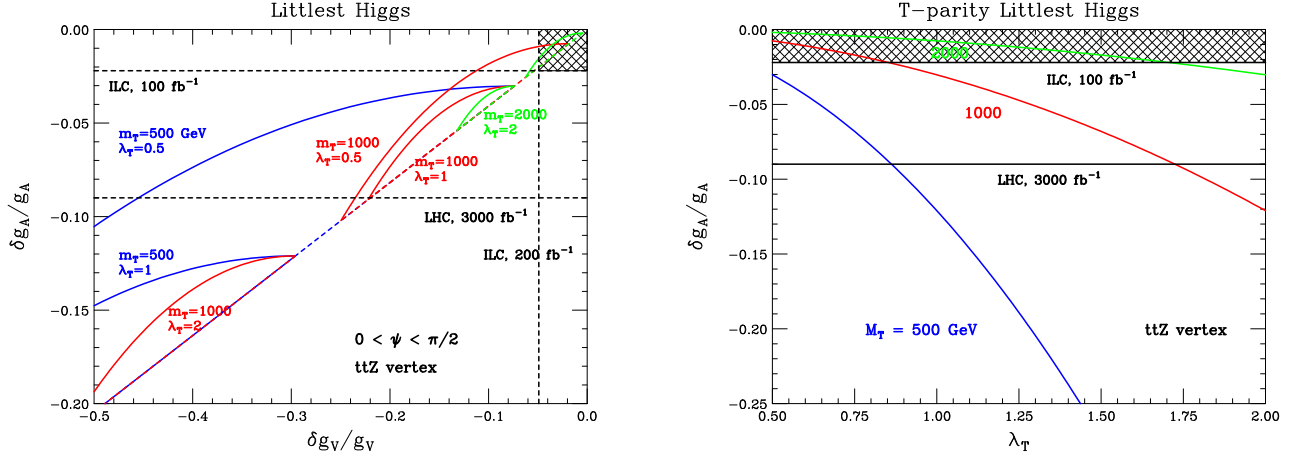


Figure 24: The corrections to the  $t\bar{t}Z$  axial and vector couplings in the original Littlest Higgs model (left panel) and its extension with T-parity (right panel). The regions in which the ILC would observe no deviation from the SM are shaded.

of the ILC. However, we will show below that the corrections to the gauge couplings of the SM top, induced by its mixing with the  $T$ , will be observable at the ILC throughout the parameter range consistent with naturalness. Measuring these corrections will provide a unique window on the top sector of the Little Higgs.

Little Higgs models contain a light Higgs boson which is a *composite* of more fundamental degrees of freedom. A generic composite Higgs model must become strongly coupled at an energy scale around 1 TeV, leading to unacceptably large corrections to precision electroweak observables. In contrast, Little Higgs models remain perturbative until a higher energy scale, around 10 TeV. The hierarchy between the Higgs mass and the strong coupling scale is natural and stable with respect to radiative corrections. Because of the special symmetry structure of the theory, the Higgs mass vanishes at tree level, as do one-loop quadratically divergent diagrams. The mass term is dominated by the logarithmically divergent one-loop contribution from the top quark, which triggers electroweak symmetry breaking.

Many Little Higgs models have been proposed in the literature. We will consider two examples in this study, the “Littlest Higgs” model [117], and its variation incorporating T parity [118]. We will study the effects on the  $t\bar{t}Z$  vertex in these models; for a more detailed study, see [114].

Corrections to the gauge couplings of the top quark in Little Higgs model arise from two sources: the mixing of the (left-handed) top with the heavy top  $T$ , and the mixing of the SM gauge bosons  $W^\pm, Z^0$  with their heavy counterparts,  $W_H^\pm$  and  $W_H^3$ . Using the superscripts “t” and “g” to denote the contributions from these two sources, the corrections to the  $t\bar{t}Z$  coupling can be written as

$$\begin{aligned} \delta g_R^{Zt} &= 0, & \delta g_R^{Zg} &= \frac{v^2}{4f^2} \frac{c_\psi^2 s_\psi^2}{c_W^2 - s_W^2} g_R^Z, \\ \delta g_L^{Zt} &= \frac{\lambda_T^2 v^2 g_A^Z}{m_T^2}, & \delta g_L^{Zg} &= \frac{v^2}{4f^2} \left[ 2g_A^Z s_\psi^4 + g_R^Z \frac{c_\psi^2 s_\psi^2}{c_W^2 - s_W^2} \right]. \end{aligned} \quad (17)$$

Here,  $g_{L,R}^Z$  are the SM left- and right-handed  $t\bar{t}Z$  couplings,  $g_V^Z = (g_R^Z + g_L^Z)/2$  and  $g_A^Z = (g_R^Z - g_L^Z)/2$  are their vector and axial combinations,  $c_W, s_W$  are respectively the cosine and sine of the weak mixing angle, and  $s_\psi \equiv \sin \psi$ ,  $c_\psi \equiv \cos \psi$ . In the original Littlest Higgs model [117], both the gauge sector shift and the top sector shift occur; in the T-parity model [118], only the top sector shift is present. The predicted shifts in the  $t\bar{t}Z$  axial and vector couplings for  $m_T = 0.5, 1.0$ , and  $2.0$  TeV, and  $\lambda_T = 0.5, 1, 2$ , are plotted in Fig. 24 (left panel), along with the experimental sensitivities expected at the LHC [10] and the ILC [9]. The mixing angle  $\psi$  is varied between 0 and  $\pi/2$ . Note that the shifts have a definite sign. While only a rather small part of the parameter space is accessible at the LHC even with  $3000 \text{ fb}^{-1}$  integrated luminosity, the ILC experiments will be able to easily observe the shifts in most of the parameter space preferred by naturalness considerations (however, the prospects for observation at

the LHC improve when additional final states such as  $b\bar{b} + 4j$  are included; see [120]). Similarly, shifts in the  $Wtb$  coupling can be probed via deviations in the top quark width at the ILC [114].

### 4.3. Testing CPT Symmetry with Top Quark Physics [121]

*J.A.R. Cembranos*

The viability to observe evidence of CPT violation in the top sector has been analyzed through the measurement of a mass difference between top and anti-top [121]. This study has been focused on the CPT violating ratio of the top quark,  $R_{CPT}(t) \equiv 2(m_t - m_{\bar{t}})/(m_t + m_{\bar{t}})$ . The present constraints from the Tevatron are approximately 10%, and they could be reduced by one order of magnitude at the LHC or ILC. The most promising studied channel is the lepton plus jets channel for top anti-top production. However, other techniques to reconstruct the top mass could also be very interesting, such as the analysis of the  $J/\psi$  from  $b$  decay at the LHC, which improves the systematics. Single top production could also be studied, since a combination of different measurements would be necessary in order to consider CPT violation as the explanation of any exotic data.

Di-lepton channel: Di-lepton events originating predominantly from  $t\bar{t} \rightarrow W^+(\rightarrow l^+\nu) b W^-(\rightarrow l^-\bar{\nu}) \bar{b}$ , with  $l = e$  or  $\mu$ , have been used in Tevatron to measure the top quark pole mass supposing an identical mass for the top and anti-top quarks. The same data can be used to study CPT violation through a double peak in the reconstructed invariant mass associated to the lepton and b quark coming from the single decay of the top or anti-top [121]. By

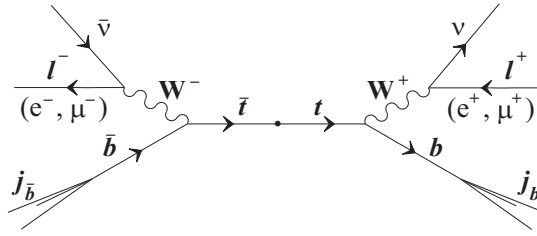


Figure 25: Schematics of the top and anti-top decays in the dilepton channel.

using the Tevatron data accumulated at Fermilab from 1992 through 1995 [122], it is possible to find the bound  $|R_{CPT}(t)| < 0.13$  at the 95% C.L. [121]. On the other hand, the sensitivity of the LHC can be estimated as  $R_{CPT}(t) = 0.03$  at the 95% c.l. following an analogous analysis [121].

Lepton plus jets channel: A more promising signal is provided when one of the  $W$  decays leptonically while the other one decays hadronically:  $t\bar{t} \rightarrow W^+(\rightarrow l^+\nu b) b W^-(\rightarrow q\bar{q}') \bar{b}$ . In fact, the inclusive lepton plus jets channel provides a larger and cleaner sample of top quarks, whose mass can be reconstructed directly using the hadronic part of the decay. The invariant mass of the three jets coming from the top ( $m_{jjb} \equiv m_{j_q j_{q'} j_b}$ ) or anti-top ( $m_{jj\bar{b}} \equiv m_{j_q j_{q'} j_{\bar{b}}}$ ) presents a peak at the top ( $m_t$ ) or anti-top ( $m_{\bar{t}}$ ) mass respectively.

The estimate combining the CDF [123] and DO data [124] gives a more constraining bound of  $R_{CPT}(t) < 9.2 \times 10^{-2}$ . The sensitivity of the LHC is also better in this channel since both statistical and systematic uncertainties are expected to be improved. Indeed, the LHC will be able to test the CPT violation of the top quark to almost one order of magnitude better than the present constraints:  $|R_{CPT}(t)| \simeq 0.014$  at the 95% C.L. or equivalently,  $m_t - m_{\bar{t}} \simeq 2.4$  GeV [121].

The same analyses can be performed with the ILC, where an increase of the statistical uncertainties but a decrease of the systematic ones is expected [125]. The importance of these last uncertainties leads to a small improvement of the sensitivity in relation to the LHC.

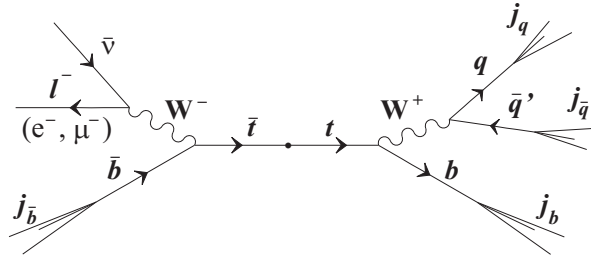


Figure 26: Schematic example of the top and anti-top decays in the lepton plus jets channel.

## ACKNOWLEDGMENTS

CFB is supported by the US Department of Energy under contract DE-AC02-76SF00515. YK is supported by the DFG Sonderforschungsbereich/Transregio 9 "Computer-gestützte Theoretische Teilchenphysik". FP is supported by the University of Wisconsin Research Committee with funds granted by the Wisconsin Alumni Research Foundation.

## References

- [1] M. Beneke *et al.*, arXiv:hep-ph/0003033.
- [2] M. Martinez and R. Miquel, *Eur. Phys. J. C* **27**, 49 (2003) [arXiv:hep-ph/0207315].
- [3] P. Batra and T. M.P. Tait, Work in progress.
- [4] F. Maltoni and T. Stelzer, *JHEP* **0302**, 027 (2003) [arXiv:hep-ph/0208156].
- [5] F. Abe *et al.* (CDF Collaboration), *Phys. Rev. Lett.* **74**, 2626 (1995).
- [6] S. Abachi *et al.* (DØ Collaboration), *Phys. Rev. Lett.* **74**, 2632 (1995).
- [7] D. Chakraborty, J. Konigsberg and D. L. Rainwater, *Ann. Rev. Nucl. Part. Sci.* **53**, 301 (2003), [arXiv:hep-ph/0303092].
- [8] F. Larios, M. A. Perez and C. P. Yuan, *Phys. Lett.* **B457**, 334 (1999); M. Frigeni and R. Rattazzi, *Phys. Lett.* **B269**, 412 (1991).
- [9] T. Abe *et al.* [American Linear Collider Working Group], in *Proc. of the APS/DPF/DPB Summer Study on the Future of Particle Physics (Snowmass 2001)* ed. N. Graf, hep-ex/0106057.
- [10] U. Baur, A. Juste, L. H. Orr and D. Rainwater, *Phys. Rev.* **D71**, 054013 (2005), [arXiv:hep-ph/0412021].
- [11] W. Hollik *et al.*, *Nucl. Phys.* **B551**, 3 (1999) [Erratum-ibid. **B557**, 407 (1999)].
- [12] ATLAS TDR, report CERN/LHCC/99-15 (1999); Ph. Schwemling, ATLAS note SN-ATLAS-2003-034.
- [13] G. Altarelli, L. Conti and V. Lubicz, *Phys. Lett.* **B502**, 125 (2001) and references therein.
- [14] U. Baur, A. Juste, L. H. Orr and D. Rainwater, arXiv:hep-ph/0512262.
- [15] Sections 2.4 and 2.6 of these Proceedings.
- [16] S. Laporta and E. Remiddi, *Phys. Lett.* **B379** (1996) 283 [hep-ph/9602417].  
S. Laporta, *Int. J. Mod. Phys. A* **15** (2000) 5087 [hep-ph/0102033].
- [17] F.V. Tkachov, *Phys. Lett.* **B100** (1981) 65.  
K.G. Chetyrkin and F.V. Tkachov, *Nucl. Phys.* **B192** (1981) 159.
- [18] T. Gehrmann and E. Remiddi, *Nucl. Phys.* **B580** (2000) 485 [hep-ph/9912329].
- [19] A. V. Kotikov, *Phys. Lett.* **B254** (1991) 158.
- [20] E. Remiddi, *Nuovo Cim.* **110A** (1997) 1435 [hep-th/9711188].
- [21] M. Caffo, H. Czyż, S. Laporta and E. Remiddi, *Acta Phys. Polon.* **B29** (1998) 2627 [hep-ph/9807119].  
M. Caffo, H. Czyż, S. Laporta and E. Remiddi, *Nuovo Cim.* **A111** (1998) 365 [hep-ph/9805118].
- [22] R. Bonciani, P. Mastrolia and E. Remiddi, *Nucl. Phys.* **B661** (2003) 289 [Erratum-ibid. *Nucl. Phys.* **B702** (2004) 259] [hep-ph/0301170].
- [23] R. Bonciani, P. Mastrolia and E. Remiddi, *Nucl. Phys.* **B690** (2004) 138 [hep-ph/0311145].

- [24] E. Remiddi and J. A. M. Vermaseren, *Int. J. Mod. Phys. A* **15** (2000) 725 [hep-ph/9905237].
- [25] T. Gehrmann and E. Remiddi, *Comput. Phys. Commun.* **141** (2001) 296 [hep-ph/0107173].
- [26] W. Bernreuther, R. Bonciani, T. Gehrmann, R. Heinesch, T. Leineweber, P. Mastrolia and E. Remiddi, *Nucl. Phys.* **B706** (2005) 245 [hep-ph/0406046].
- [27] W. Bernreuther, R. Bonciani, T. Gehrmann, R. Heinesch, T. Leineweber, P. Mastrolia and E. Remiddi, *Nucl. Phys.* **B712** (2005) 229 [hep-ph/0412259].
- [28] W. Bernreuther, R. Bonciani, T. Gehrmann, R. Heinesch, T. Leineweber and E. Remiddi, *Nucl. Phys.* **B723** (2005) 93 [hep-ph/0504190].
- [29] W. Bernreuther, R. Bonciani, T. Gehrmann, R. Heinesch, P. Mastrolia and E. Remiddi, *Phys. Rev.* **D72** (2005) 096002 [hep-ph/0508254].
- [30] U. Baur, M. Buice and L.H. Orr, *Phys. Rev.* **D64** (2001) 094019 [hep-ph/0106341].
- [31] U. Baur, section 2.2 of this report
- [32] J.A. Aguilar-Saavedra et al. [ECFA/DESY LC Physics Working Group Collaboration], hep-ph/0106315.
- [33] A. Juste, section 2.5 of this report, arXiv:hep-ph/0512246, and this Proceedings ALCPG0426.
- [34] W. Bernreuther, R. Bonciani, T. Gehrmann, R. Heinesch, T. Leineweber, P. Mastrolia and E. Remiddi, *Phys. Rev. Lett.* **95**, 261802 (2005) [hep-ph/0509341].
- [35] R. Escribano and E. Masso, *Nucl. Phys.* **B429** (1994) 19 [hep-ph/9403304].
- [36] B. Grzadkowski, J. H. Kuhn, P. Krawczyk and R. G. Stuart, *Nucl. Phys. B* **281**, 18 (1987).
- [37] R. J. Guth and J. H. Kuhn, *Nucl. Phys. B* **368**, 38 (1992).
- [38] W. Kummer and W. Modritsch, *Phys. Lett. B* **349**, 525 (1995) [arXiv:hep-ph/9501406].
- [39] J. H. Kuhn, *Acta Phys. Polon. B* **12**, 347 (1981).
- [40] V. S. Fadin and V. A. Khoze, *JETP Lett.* **46**, 525 (1987) [*Pisma Zh. Eksp. Teor. Fiz.* **46**, 417 (1987)].
- [41] A. H. Hoang and C. J. Reisser, *Phys. Rev. D* **71**, 074022 (2005) [arXiv:hep-ph/0412258].
- [42] K. Melnikov and O. I. Yakovlev, *Phys. Lett. B* **324**, 217 (1994) [arXiv:hep-ph/9302311].
- [43] V. S. Fadin, V. A. Khoze and A. D. Martin, *Phys. Rev. D* **49**, 2247 (1994).
- [44] K. J. F. Gaemers and G. J. Gounaris, *Phys. Lett. B* **77**, 379 (1978); A. Djouadi, J. Kalinowski and P. M. Zerwas, *Mod. Phys. Lett. A* **7**, 1765 (1992); A. Djouadi, J. Kalinowski and P. M. Zerwas, *Z. Phys. C* **54**, 255 (1992).
- [45] S. Dawson and L. Reina, *Phys. Rev. D* **57**, 5851 (1998) [arXiv:hep-ph/9712400].
- [46] S. Dawson and L. Reina, *Phys. Rev. D* **59**, 054012 (1999) [arXiv:hep-ph/9808443].
- [47] S. Dittmaier, M. Kramer, Y. Liao, M. Spira and P. M. Zerwas, *Phys. Lett. B* **441**, 383 (1998) [arXiv:hep-ph/9808433].
- [48] G. Belanger *et al.*, *Phys. Lett. B* **571**, 163 (2003) [arXiv:hep-ph/0307029].
- [49] A. Denner, S. Dittmaier, M. Roth and M. M. Weber, *Nucl. Phys. B* **680**, 85 (2004) [arXiv:hep-ph/0309274].
- [50] Y. You, W. G. Ma, H. Chen, R. Y. Zhang, S. Yan-Bin and H. S. Hou, *Phys. Lett. B* **571**, 85 (2003) [arXiv:hep-ph/0306036].
- [51] C. Farrell and A. H. Hoang, *Phys. Rev. D* **72**, 014007 (2005) [arXiv:hep-ph/0504220]; C. Farrell and A. H. Hoang, arXiv:hep-ph/0506253.
- [52] A. Pineda and J. Soto, *Nucl. Phys. Proc. Suppl.* **64**, 428 (1998); M. E. Luke, A. V. Manohar and I. Z. Rothstein, *Phys. Rev. D* **61**, 074025 (2000) [arXiv:hep-ph/9910209].
- [53] A. Juste, arXiv:hep-ph/0512246 and this Proceedings ALCPG0426.
- [54] G. Weiglein *et al.* [LHC/LC Study Group], arXiv:hep-ph/0410364.
- [55] A. Juste and G. Merino, arXiv:hep-ph/9910301; A. Gay, results presented at the 2nd ECFA/DESY Workshop, Saint Malo, France, April 12-15, 2002.
- [56] A. Juste, results presented at the Chicago Linear Collider Workshop, Chicago, USA, January 2002, <http://www.pas.rochester.edu/~orr/justelc.pdf>.
- [57] G. Moortgat-Pick *et al.*, arXiv:hep-ph/0507011.
- [58] A. H. Hoang and T. Teubner, *Phys. Rev. D* **60**, 114027 (1999) [arXiv:hep-ph/9904468]; K. Melnikov and A. Yelkhovsky, *Nucl. Phys. B* **528**, 59 (1998) [arXiv:hep-ph/9802379]; O. I. Yakovlev, *Phys. Lett. B* **457**,

- 170 (1999) [arXiv:hep-ph/9808463]; M. Beneke, A. Signer and V. A. Smirnov, Phys. Lett. B **454**, 137 (1999) [arXiv:hep-ph/9903260]; T. Nagano, A. Ota and Y. Sumino, Phys. Rev. D **60**, 114014 (1999) [arXiv:hep-ph/9903498]; A. A. Penin and A. A. Pivovarov, Phys. Atom. Nucl. **64**, 275 (2001) [arXiv:hep-ph/9904278].
- [59] B. Kniehl, A. Penin, V. Smirnov and M. Steinhauser, Nucl. Phys. **B635**, 357 (2002).
- [60] M. Beneke, Y. Kiyo and K. Schuller, Nucl. Phys. **B714**, 67 (2005).
- [61] B. Kniehl and A. Penin, Nucl. Phys. **B563**, 200 (1999);  
A. Penin and M. Steinhauser, Phys. Lett. **B538**, 335 (2002).
- [62] Y. Kiyo and Y. Sumino, Phys. Rev. **D67**, 071501 (2003), and references therein.
- [63] A. V. Manohar, J. Soto and I. W. Stewart, Phys. Lett. **B486**, 400 (2000);  
A. Hoang and I. W. Stewart, Phys. Rev. **D67**, 114020 (2003).
- [64] A. H. Hoang, A. V. Manohar, I. W. Stewart and T. Teubner, Phys. Rev. Lett. **86**, 1951 (2001); Phys. Rev. **D65**, 014014 (2002), and references therein.
- [65] A. H. Hoang, Phys. Rev. **D69**, 034009 (2004); Acta Phys. Polon. **B34**, 4491 (2003).
- [66] A. H. Hoang and T. Teubner, Phys. Rev. **D60**, 114027 (1999).
- [67] T. Nagano, A. Ota and Y. Sumino, Phys. Rev. **D60**, 114014 (1999).
- [68] R. Harlander, M. Jezabek, J. H. Kuhn and M. Peter, Z. Phys. **C73**, 477 (1997).
- [69] M. Peter and Y. Sumino, Phys. Rev. **D57**, 6912 (1998).
- [70] V. S. Fadin, V. A. Khoze and M. I. Kotsky, Z. Phys. **C64**, 45 (1994);  
R. Harlander, M. Jezabek, J. H. Kuhn and T. Teubner, Phys. Lett. **B346**, 137 (1995);  
M. Jezabek, T. Nagano and Y. Sumino, Phys. Rev. **D62**, 014034 (2000).
- [71] S. T. Boogert and D. J. Miller, in the proceedings of LCWS 2002 (Jeju Island, Korea, August 2002), *Seogwipo 2002, Linear colliders, 509-516*, arXiv:hep-ex/0211021, and references therein.
- [72] A. Hinze and K. Monig, arXiv:physics/0506115.
- [73] K. Monig, "Measurement of the differential luminosity using Bhabha events in the forward tracking region at TESLA", LC-PHSM-2000-060.
- [74] A. A. Penin, Phys. Rev. Lett. **95**, 010408 (2005); Nucl. Phys. **B734**, 185 (2006);  
R. Bonciani and A. Ferroglia, Phys. Rev. **D72**, 056004 (2005);  
S. A. Yost, S. Majhi and B. F. L. Ward, talk at Loopfest IV, Snowmass05, arXiv:hep-ph/0512022.
- [75] O. Biebel, Phys. Rept. **340** (2001) 165;  
S. Bethke, Phys. Rept. **403** (2004) 203 [hep-ex/0406058].
- [76] A. Gehrmann-De Ridder, T. Gehrmann and E.W.N. Glover, JHEP **0509** (2005) 056 [hep-ph/0505111].
- [77] J. Campbell, M.A. Cullen and E.W.N. Glover, Eur. Phys. J. C **9** (1999) 245 [hep-ph/9809429].
- [78] D.A. Kosower, Phys. Rev. D **57** (1998) 5410 [hep-ph/9710213]; Phys. Rev. D **71** (2005) 045016 [hep-ph/0311272].
- [79] S. Catani and M.H. Seymour, Nucl. Phys. B **485** (1997) 291; **510** (1997) 503(E) [hep-ph/9605323].
- [80] W.T. Giele and E.W.N. Glover, Phys. Rev. D **46** (1992) 1980;  
Z. Kunszt and D.E. Soper, Phys. Rev. D **46** (1992) 192;  
S. Frixione, Z. Kunszt and A. Signer, Nucl. Phys. B **467** (1996) 399 [hep-ph/9512328]; Z. Nagy and Z. Trocsanyi, Nucl. Phys. B **486** (1997) 189 [hep-ph/9610498].
- [81] D.A. Kosower, Phys. Rev. D **67** (2003) 116003 [hep-ph/0212097].
- [82] S. Weinzierl, JHEP **0303** (2003) 062 [hep-ph/0302180];  
W.B. Kilgore, Phys. Rev. D **70** (2004) 031501 [hep-ph/0403128];  
M. Grazzini and S. Frixione, JHEP **0506** (2005) 010 [hep-ph/0411399];  
G. Somogyi, Z. Trocsanyi and V. Del Duca, JHEP **0506** (2005) 024 [hep-ph/0502226].
- [83] A. Gehrmann-De Ridder and E.W.N. Glover, Nucl. Phys. B **517** (1998) 269 [hep-ph/9707224];  
J. Campbell and E.W.N. Glover, Nucl. Phys. B **527** (1998) 264 [hep-ph/9710255];  
S. Catani and M. Grazzini, Phys. Lett. B **446** (1999) 143 [hep-ph/9810389]; Nucl. Phys. B **570** (2000) 287 [hep-ph/9908523];

- F.A. Berends and W.T. Giele, Nucl. Phys. B **313** (1989) 595;  
V. Del Duca, A. Frizzo and F. Maltoni, Nucl. Phys. B **568** (2000) 211 [hep-ph/9909464].
- [84] Z. Bern, L.J. Dixon, D.C. Dunbar and D.A. Kosower, Nucl. Phys. B **425** (1994) 217 [hep-ph/9403226];  
D.A. Kosower, Nucl. Phys. B **552** (1999) 319 [hep-ph/9901201];  
D.A. Kosower and P. Uwer, Nucl. Phys. B **563** (1999) 477 [hep-ph/9903515];  
Z. Bern, V. Del Duca and C.R. Schmidt, Phys. Lett. B **445** (1998) 168 [hep-ph/9810409];  
Z. Bern, V. Del Duca, W.B. Kilgore and C.R. Schmidt, Phys. Rev. D **60** (1999) 116001 [hep-ph/9903516].
- [85] A. Gehrmann-De Ridder, T. Gehrmann and E.W.N. Glover, Nucl. Phys. B **691** (2004) 195 [hep-ph/0403057].
- [86] A. Gehrmann-De Ridder, T. Gehrmann and E.W.N. Glover, Phys. Lett. B **612** (2005) 36 [hep-ph/0501291].
- [87] H.E. Haber and D. Wyler, Nucl. Phys. B **323** (1989) 267.
- [88] A. Gehrmann-De Ridder, T. Gehrmann and E.W.N. Glover, Phys. Lett. B **612** (2005) 49 [hep-ph/0502110].
- [89] F. Wilczek, Phys. Rev. Lett. **39** (1977) 1304;  
M.A. Shifman, A.I. Vainshtein and V.I. Zakharov, Phys. Lett. B **78** (1978) 443.
- [90] A. Gehrmann-De Ridder, T. Gehrmann and G. Heinrich, Nucl. Phys. B **682** (2004) 265 [hep-ph/0311276].
- [91] A. Gehrmann-De Ridder, T. Gehrmann and E. W. N. Glover, Nucl. Phys. Proc. Suppl. **135** (2004) 97 [hep-ph/0407023].
- [92] K. Hagiwara and D. Zeppenfeld, Nucl. Phys. B **313** (1989) 560;  
F.A. Berends, W.T. Giele and H. Kuijff, Nucl. Phys. B **321** (1989) 39;  
N.K. Falck, D. Graudenz and G. Kramer, Nucl. Phys. B **328** (1989) 317.
- [93] Z. Bern, L.J. Dixon, D.A. Kosower and S. Weinzierl, Nucl. Phys. B **489** (1997) 3 [hep-ph/9610370];  
Z. Bern, L.J. Dixon and D.A. Kosower, Nucl. Phys. B **513** (1998) 3 [hep-ph/9708239];  
E.W.N. Glover and D.J. Miller, Phys. Lett. B **396** (1997) 257 [hep-ph/9609474];  
J.M. Campbell, E.W.N. Glover and D.J. Miller, Phys. Lett. B **409** (1997) 503 [hep-ph/9706297];  
Z. Nagy and Z. Trocsanyi, Phys. Lett. B **414** (1997) 187 [hep-ph/9708342].
- [94] L.W. Garland, T. Gehrmann, E.W.N. Glover, A. Koukoutsakis and E. Remiddi, Nucl. Phys. B **627** (2002) 107 [hep-ph/0112081] and **642** (2002) 227 [hep-ph/0206067].
- [95] A. Gehrmann-De Ridder, T. Gehrmann, E.W.N. Glover and G. Heinrich, work in progress.
- [96] S. Godfrey and S. h. Zhu, arXiv:hep-ph/0511329 and this Proceedings ALCPG0427.
- [97] T. Han, D. L. Rainwater and G. Valencia, Phys. Rev. D **68**, 015003 (2003) [arXiv:hep-ph/0301039].
- [98] S. Godfrey and S. h. Zhu, Phys. Rev. D **72**, 074011 (2005) [arXiv:hep-ph/0412261].
- [99] R. Cahn and S. Dawson, Phys. Lett. **136B**, 196 (1984); (E) Phys. Lett. **138B**, 464 (1984); S. Dawson, Nucl. Phys. B **249**, 42 (1985); M. Chanowitz and M. Gaillard, Phys. Lett. **142B**, 85 (1984); G. Kane, W. Repko, and W. Rolnick, Phys. Lett. **148B**, 367 (1984); J. Lindfors, Z. Phys. C **28**, 427 (1985).
- [100] S. Dawson and S. S. D. Willenbrock, Nucl. Phys. B **284**, 449 (1987).
- [101] R. P. Kauffman, Phys. Rev. D **41**, 3343 (1990).
- [102] T. Hahn, Nucl. Phys. Proc. Suppl. **89**, 231 (2000) [arXiv:hep-ph/0005029] and references therein.
- [103] For more details, see Zack Sullivan, arXiv:hep-ph/0509012 and this Proceedings ALCPG0402.
- [104] L. Randall and R. Sundrum, Phys. Rev. Lett. **83**, 3370 (1999) [arXiv:hep-ph/9905221]; L. Randall and R. Sundrum, Phys. Rev. Lett. **83**, 4690 (1999) [arXiv:hep-th/9906064].
- [105] H. Davoudiasl, J. L. Hewett and T. G. Rizzo, Phys. Lett. B **473**, 43 (2000) [arXiv:hep-ph/9911262]; A. Pomarol, Phys. Lett. B **486**, 153 (2000) [arXiv:hep-ph/9911294].
- [106] Y. Grossman and M. Neubert, Phys. Lett. B **474**, 361 (2000) [arXiv:hep-ph/9912408].
- [107] T. Gherghetta and A. Pomarol, Nucl. Phys. B **586**, 141 (2000) [arXiv:hep-ph/0003129].
- [108] S. J. Huber and Q. Shafi, Phys. Lett. B **498**, 256 (2001) [arXiv:hep-ph/0010195]; S. J. Huber, Nucl. Phys. B **666**, 269 (2003) [arXiv:hep-ph/0303183].
- [109] S. J. Huber and Q. Shafi, Phys. Rev. D **63**, 045010 (2001) [arXiv:hep-ph/0005286]; S. J. Huber, C. A. Lee and Q. Shafi, Phys. Lett. B **531**, 112 (2002) [arXiv:hep-ph/0111465]; C. Csaki, J. Erlich and J. Terning, Phys. Rev. D **66**, 064021 (2002) [arXiv:hep-ph/0203034]; J. L. Hewett, F. J. Petriello and T. G. Rizzo, JHEP **0209**, 030

- (2002) [arXiv:hep-ph/0203091].
- [110] K. Agashe, A. Delgado, M. J. May and R. Sundrum, JHEP **0308**, 050 (2003) [arXiv:hep-ph/0308036].
- [111] J. M. Maldacena, Adv. Theor. Math. Phys. **2**, 231 (1998) [Int. J. Theor. Phys. **38**, 1113 (1999)] [arXiv:hep-th/9711200]; S. S. Gubser, I. R. Klebanov and A. M. Polyakov, Phys. Lett. B **428**, 105 (1998) [arXiv:hep-th/9802109]; E. Witten, Adv. Theor. Math. Phys. **2**, 253 (1998) [arXiv:hep-th/9802150].
- [112] N. Arkani-Hamed, M. Porrati and L. Randall, JHEP **0108**, 017 (2001) [arXiv:hep-th/0012148]; R. Rattazzi and A. Zaffaroni, JHEP **0104**, 021 (2001) [arXiv:hep-th/0012248].
- [113] For recent reviews and more references, see M. Schmaltz and D. Tucker-Smith, arXiv:hep-ph/0502182; M. Perelstein, arXiv:hep-ph/0512128.
- [114] For more details, see C. F. Berger, M. Perelstein and F. Petriello, arXiv:hep-ph/0512053 and this Proceedings ALCPG0428.
- [115] M. Perelstein, M. E. Peskin and A. Pierce, Phys. Rev. D **69**, 075002 (2004) [arXiv:hep-ph/0310039].
- [116] G. Azuelos *et al.*, Eur. Phys. J. C **39S2**, 13 (2005) [arXiv:hep-ph/0402037].
- [117] N. Arkani-Hamed, A. G. Cohen, E. Katz and A. E. Nelson, JHEP **0207**, 034 (2002) [arXiv:hep-ph/0206021].
- [118] H. C. Cheng and I. Low, JHEP **0309**, 051 (2003) [arXiv:hep-ph/0308199]; I. Low, JHEP **0410**, 067 (2004) [arXiv:hep-ph/0409025].
- [119] C. Csaki, J. Hubisz, G. D. Kribs, P. Meade and J. Terning, Phys. Rev. D **67**, 115002 (2003) [arXiv:hep-ph/0211124]; J. L. Hewett, F. J. Petriello and T. G. Rizzo, JHEP **0310**, 062 (2003) [arXiv:hep-ph/0211218].
- [120] Section 2.2 of these Proceedings and U. Baur, A. Juste, D. Rainwater and L. H. Orr, arXiv:hep-ph/0512262.
- [121] For more details, see J. A. R. Cembranos, A. Rajaraman and F. Takayama, arXiv:hep-ph/0512020 and this Proceedings ALCPG0410; in preparation.
- [122] F. Abe *et al.*, CDF Collaboration, Phys. Rev. Lett. **80**, 2779 (1998)
- [123] F. Abe *et al.*, CDF Collaboration, Phys. Rev. Lett. **80**, 2767 (1998)
- [124] B. Abbott *et al.*, DØ Collaboration, Phys. Rev. D **58**, 052001 (1998); Phys. Rev. Lett. **79**, 1197 (1997)
- [125] A. Biernacik, K. Kolodziej, A. Lorca and T. Riemann, Acta Phys. Polon. B **34**, 5487 (2003)